SEGMENTATION OF HUMAN FACIAL MUSCLES ON CT AND MRI DATA USING LEVEL SET AND BAYESIAN METHODS

A THESIS SUBMITTED TO
THE GRADUATE SCHOOL OF INFORMATICS
OF
THE MIDDLE EAST TECHNICAL UNIVERSITY

BY

HİKMET EMRE KALE

IN PARTIAL FULFILLMENT OF THE REQUIREMENTS FOR THE DEGREE OF
MASTER OF SCIENCE
IN
THE DEPARTMENT OF HEALTH INFORMATICS

JUNE 2011

Approval of the Graduate School of Informatics

Prof. Dr. Nazife BAYKAL
Director

I certify that this thesis satisfies all the requirements as a thesis for the degree of Master of Science.

Assist. Prof. Dr. Didem GÖKÇAY
Head of Department

This is to certify that we have read this thesis and that in our opinion it is fully adequate, in scope and quality, as a thesis for the degree of Master of Science.

Assoc. Prof. Dr. Erkan MUMCUOĞLU
Supervisor

Examining Committee Members

Prof. Dr. Fatoş Tünay YARMAN VURAL	(METU, CENG)
Assoc. Prof. Dr. Ü. Erkan MUMCUOĞLU	(METU, II)
Assist. Prof. Dr. Didem GÖKÇAY	(METU, II)
Assist. Prof. Dr. Alptekin TEMİZEL	(METU, II)
Prof. Dr. Yasemin YARDIMCI	(METU, II)

I hereby declare that all information in this document has been obtained and presented in accordance with academic rules and ethical conduct. I also declare that, as required by these rules and conduct, I have fully cited and referenced all material and results that are not original to this work.

Name, Last Name: **Hikmet Emre Kale**

Signature :

ABSTRACT

SEGMENTATION OF HUMAN FACIAL MUSCLES ON CT AND MRI DATA USING LEVEL SET AND BAYESIAN METHODS

Kale, Hikmet Emre
M.S., Department of Health Informatics
Supervisor : Assoc. Prof. Dr. Erkan MUMCUOĞLU

June 2011, 77 pages

Medical image segmentation is a challenging problem, and is studied widely. In this thesis, the main goal is to develop automatic segmentation techniques of human mimic muscles and to compare them with ground truth data in order to determine the method that provides best segmentation results. The segmentation methods are based on Bayesian with Markov Random Field (MRF) and Level Set (Active Contour) models. Proposed segmentation methods are multi step processes including preprocess, main muscle segmentation step and post process, and are applied on three types of data: Magnetic Resonance Imaging (MRI) data, Computerized Tomography (CT) data and unified data, in which case, information coming from both modalities are utilized. The methods are applied both in three dimensions (3D) and two dimensions (2D) data cases. A simulation data and two patient data are utilized for tests. The patient data results are compared statistically with ground truth data which was labeled by an expert radiologist.

Keywords: Medical Image Segmentation, Level Sets, Bayesian Methods, Markov Random Fields

ÖZ

İNSAN YÜZ KASLARININ KESİT KÜMESİ VE BAYESÇİ YÖNTEMLERLE MANYETİK REZONANS VE BİLGİSAYARLI TOMOGRAFİ VERİSİ KULLANILARAK BÖLÜTLENMESİ

Kale, Hikmet Emre
Yüksek Lisans, Sağlık Bilişimi Bölümü
Tez Yöneticisi : Doç. Dr. Erkan MUMCUOĞLU

Haziran 2011, 77 sayfa

Tıbbi görüntü bölütleme pek çok zorluklar içerir ve üzerinde sıklıkla çalışılan bir problemdir. Bu tezin ana hedefi insan mimik kaslarını otomatik olarak bölütlemek için yöntemler geliştirmek ve bu yöntemleri karşılaştırarak en iyi yöntemi belirlemektir. Bölütleme yöntemleri Bayesçi Markov Rastgele Alanlar ve Etkin Çevre Hatları modelleri üzerine kurulmuştur. Önerilen bölütleme yöntemleri ön işleme, ana kas bölütleme işlemi ve son işlem kısımlarını içeren birden çok basamaklı birer işlemdir. Yöntemler Manyetik Rezonans (MR), Bilgisayarlı Tomografi (BT) verisi ve bilginin her iki veriden de geldiği birleştirilmiş veri seti üzerinde uygulandı. Yöntemler hem iki boyutlu hem üç boyutlu olarak uygulandı. Hasta verisinden elde edilen sonuçlar uzman bir radyolog tarafından işaretlenmiş kaslarla istatistiki olarak karşılaştırıldı.

Anahtar Kelimeler: Tıbbi Görüntü Bölütleme, Kesit Kümesi Yöntemi, Bayesçi Yöntemler, Markov Rastgele Alanlar

To My Family

ACKNOWLEDGMENTS

I express sincere appreciation to my supervisor Assoc. Prof. Dr. Erkan Mumcuoğlu for his patience guidance throughout the research. I greatly appreciate his share in every step in the development of the thesis.

Thanks go to Dr. Salih Hamcan for labeling images for the ground truth data and Dr. Fatih Örs for providing MR and CT images.

I am deeply grateful to my friend Emre Şener for sharing his knowledge and for his guidance during the Tübitak 1001 Project and this thesis.

I would also gratefully thank to my parents, my father Cahit Kale and my mother Süheyla Kale -to whom i owe everything- for their patience in this long M.S. period, for their support in all kind of manner and for making my life easier. Their insight and support always helped me a lot.

I would also like to thank to my brother, Enderay Kale for supporting and motivating me. I am grateful that he always listens to me patiently and gives wise advices to me.

My friends, Ferit Üzer and Mehmet Akif Antepli's helps while editing the thesis and their support are also gratefully appreciated.

I also thank to my friend İlker Kocamış, with whom we have grown up together and share many things with each other, for motivating me.

TABLE OF CONTENTS

CHAPTERS

APPENDICES

LIST OF TABLES

LIST OF FIGURES

LIST OF ABBREVIATIONS

2D	Two Dimensional
3D	Three Dimensional
4D	Four Dimensional
Adaptive	Thickness adaptive model
ANN	Artificial Neural Network
CAD	Computer Aided Diagnosis
CFL	Courant-Freidreichs-Lewy
CT	Computerized Tomography
DC	Dice Coefficient
ENO	Essentially Non-Oscillatory
FE	Forward Euler
GAC	Geodesic Active Contour
GATA	Gülhane Askeri Tıp Akademisi
HJ	Hamilton-Jacobi
HJ ENO	Hamilton-Jacobi Essentially Non-Oscillatory Schemes
HJ WENO	Hamilton-Jacobian Weighted Essentially Non-Oscillatory Scheme
HU	Hounsfield Units
ICM	Iterated Conditional Model
kNN	k Nearest Neighbors
LS	Level Set

MAP	Maximum Aposteriori
METU	Middle East Technical University
ML	Maximum Likelihood
MR	Magnetic Resonance
MRF	Markov Random Field
MRI	Magnetic Resonance Imaging
N	No
PV	Partial Volume
RMSSSD	Root Mean Squared Symmetric Surface Distance
ROI	Region of Interest
RVFBI	Removing Voxels on the Fat Bone Interface
Standard-a	Standard Level Set model with automatically calculated class means
Standard-p	Standard Level Set model with predefine class means
SVM	Support Vector Machine
TÜBİTAK	Türkiye Bilimsel ve Teknolojik Araştırma Kurumu
WENO	Weighted Essentially Non-Oscillatory
Y	Yes

CHAPTER 1

INTRODUCTION

1.1 Scope and Motivation

In this thesis, the main objective is to develop automatic segmentation methods to segment the muscles in human face, especially the mimic muscles. This segmentation can be used to construct a more realistic human face model.

Using three dimensional (3D) MRI and CT images (as well as photographic pictures), it is possible to create a person specific face model that has the same mimics as the person. To achieve this, it is necessary to segment different tissue types and to model the biomechanical characteristics of the soft-tissue. This idea was the subject of the Türkiye Bilimsel ve Teknolojik Araştırma Kurumu (TÜBİTAK) 1001 [1] project as a collaboration of teams from Middle East Technical University (METU) Electrical Engineering, Informatics Institute, Mechanical Engineering and Gülhane Askeri Tıp Akademisi (GATA).

In computer graphics applications and in medicine, this realistic model can be useful. For example, plastic surgeon will be able to see the results of the operation she/he has planned and then with this feedback will be able to change the operation plan in computer on the model. This model can even be used to train surgeons.

A good segmentation of the face is prerequisite for this aim, which is unfortunately not easy. There are many muscles on the face that plays important roles in emotional reactions (laughing, smiling, being angry, being nervous, ...), talking and eating. These muscles in the face are very thin, often touching each other and geometrically complicated. There are also other challenges like image noise (for both MRI and CT), MRI non-uniformity (bias) [2], in which case, average tissue intensity can slowly change spatially. Another problem is that data contains partial volume voxels. It means that in the boundary of different tissue types, there are voxels which have intensities in between two tissue mean values. These make the muscle segmentation a challenging problem. There are very few publications on this subject. [3][4] are developed mainly for brain studies, but also segmentation of classes muscle, fat, bone and air exist. However, they are not applicable for facial tissue segmentation like mimic muscles. In [5] and [6] the technical details about segmentation techniques (mostly semi-automatic) were not described clearly.

1.2 Image Segmentation

Image segmentation involves both pattern recognition and image processing techniques. Image segmentation is to separate image into meaningful partitions using image processing methods and/or pattern recognition techniques. Image processing and pattern recognition techniques are used to extract information from a given image. Basic image processing techniques are, morphological operations, histogram based techniques, edge detection, etc. Pattern recognition techniques try to classify the image in feature space by using the knowledge learned in training phase or prior knowledge provided by the user. Artificial Neural Networks (ANNs), k-nearest neighbors (kNN) method and Support Vector Machines (SVMs) are examples of pattern recognition techniques. Features can be anything defining the class. Image processing techniques are also used to form the features.

Segmentation is very important in many fields like robotics, medicine and security. In medicine, image segmentation can be used in computer aided diagnosis (CAD) methods. CAD methods can automatically detect structures like tumor in brain. In addition, it is often necessary to calculate the volume of a specific organ (such as liver) or to calculate the thickness of a tissue (such as gray matter in brain) for diagnosis. These tasks are not easy to do manually by the practitioner. Because a doctor has to label every single pixel one-by-one. This procedure is difficult to achieve for anatomically complex structures or big organs like liver. So, in these kinds of applications, full automatic or semi-automatic methods are needed to help the practitioner. In full automatic segmentation methods, user just run the program and uses the segmentation result given by program (no extra effort is needed). In semi-automatic methods, the program has an interface helping user to do the segmentation [7]. This help is not only in the level of user interface but also it has segmentation algorithms to make process easier. These semi-automatic tools can be real time and respond to the acts of user and run the segmentation algorithm using the information provided by the user [7], or can do a initial segmentation and then algorithm expect user to correct the segmentation.

For image segmentation, well known pattern recognition methods like ANNs (Artificial Neural Network) can not be used in general, because training such systems needs many pre-segmented ground truth data. In this study, there are not enough labeled ground truth data to train a learning system, since obtaining CT and MR volumes of the same patient is difficult. Therefore other kinds of algorithms which depends on the intensity values should be considered. For example, watershed introduced in [8] uses gradient information of the image and can be considered as a threshold method. The drawback of this algorithm is that it might over-segment the image i.e. it finds many small partitions and a user aided merging algorithm is needed. Region growing algorithms can also be used. In these kinds of methods, regions to be segmented are assumed to have similar values of intensity and each region is expanding from a pre-assigned seed point. As a disadvantage leakage occurs and it is difficult to handle partial volume effects [9]. Also, seed points are required that makes the method semi-automatic. A basic model is suggested in [10].

Bayesian methods are also becoming very popular for image segmentation recently. If all the classes are assumed to have equal prior probabilities, this is a maximum-likelihood (ML) estimate. Each voxel is classified according to its likelihood value. The label that makes likelihood value maximum becomes the class label. This is same as the the basic histogram thresholding method. But the threshold value is determined by the given class parameters like class variances and means. As stated in [11], the main drawback is that the spatial information is discarded totally. Markov Random Field (MRF) models can be used to alleviate this problem. In a Bayesian model, if the prior is counted in the model, then the method is called Maximum A Posteriori (MAP). Neighborhood information can be used as prior information. This prior is called Gibbs prior [2] and is a very important part of the model which eliminates noise and provides connectivity. A partial volume model using MAP with Gibbs prior which includes partial volumes as different classes is proposed in [2]. They applied this model on the brain data.

In this thesis, Bayesian MRF model was implemented with some modifications to the above method, and tested thoroughly. Results and summary of the model is given in this thesis. This model was chosen because: (i) it handles partial volumes; (ii) it has a term to keep voxels connected; and (iii) it is easy to apply to vector valued images. However, this model lacks edge information, and because of the connectivity term, thin structures (including muscles) vanish in the resultant labeled image.

In medical segmentation applications, deformable models are widely used. Deformable models were first introduced in [12]. In these models, curve evolves to minimize a cost function. In image processing applications this cost function can be function of both internal and external forces. Internal forces are geometric regularization terms, and external forces are forces depending on the intensity values. In late 1980's Osher and Sethian introduced the level set framework [13]. They used Euler-Lagrange equations to solve the deformable model. This model has been widely accepted since the model handles intrinsically topological changes and easy to implement. In the same decade Mumford-Shah segmentation and denoising model was developed [14]. It is based on variational methods and minimization of an energy functional. It is a complex model to solve, Chan and Vese have simplified the model and solved using level set framework [15]. Here authors did not use any edge information so they called active contours without edges. In 1993, Casselles developed the geometric active contour model [16]. Also, in 1994, a similar model was used by Malladi [17]. This was a non-variational approach to the edge problem. In [18] Casselles et. al. modified the model using variational framework and developed geodesic active contours (GACs) which gives better results than geometric model in most of the cases as emphasized in [19].

In this study, in addition to Bayesian methods, a unified active contour model [19][20] that combines Geodesic model and Chan-Vese model is used. The model introduced in [19] and [20] is for scalar valued images. Our proposed model is a modified version to apply for vector valued images.

1.3 Source of Data

The radiological data set that was used for tests includes volumetric MRI and CT images of two patients. MRI data has 256x256x275 voxels and voxels are 8 bits. The CT data has 512x512x288 voxels and each voxel is 16 bits. To obtain unified data, CT image was registered to the MRI data using non-rigid registration technique [21]. The acquisition parameters and specifications of the data are provided in Appendix A. The final CT data has 8 bit voxels and has the same voxel size as MRI. Typically MRI data has non-uniformity caused by magnetic field during data acquisition process. Therefore, class means vary spatially. If we consider that segmentation methods mainly rely on intensity values, it is a big problem. In this thesis this non-uniformity was corrected using open source N3 [22] algorithm implementation. The code was implemented as a test class for ITK (Insight Tool Kit) [23]. The code was compiled using Microsoft Visual Studio 8 (R).

Sixteen regions from two data sets were selected to test methods. In region 1, Levator laabi superior, buccinator (partial), zygomaticus major/minor and ductus parotidis: in region 2, maseter, buccinator and zygomaticus major/minor; in region 3, Buccinator, zygomaticus, maseter and mandibula; in region 4, buccinator, zygomaticus and maseter; in regions 5, 6 and 7, orbicularis oculi; lastly in regions 8 to 16, zygomatic bone, maxillar bone and orbicularis oculi structures exists.

The ground truth data was provided by GATA radiological department, using an interactive tool that was developed in [24]. Manual segmentation is applied on both CT and MR volumes by an expert.

1.4 Contributions

In the literature, there are no published papers on automatic segmentation of human facial tissue (nor mimics muscles). In this thesis, adaptive segmentation model for both Bayesian and Level Set models are developed with some modifications to the previous models. Bayesian model was chosen because: (i) it handles partial volumes; (ii) it has a term to keep voxels connected; and (iii) it is easy to apply to vector valued images. However, this model lacks edge information, and because of the connectivity term, thin structures (including muscles) vanish in the resultant labeled image. Level Set framework applied is based on a unified active contour model [19][20] that combines Geodesic and Chan-Vese models. The model introduced in [19] and [20] was for scalar valued images. Our proposed model is a modified version to apply for vector valued images. Both method take into account the thickness of structures to be segmented and have a post process part (to get rid of voxels which are misclassified as muscles). Proposed segmentation methods are applied on three image types: Magnetic Resonance Imaging (MRI), Computerized Tomography (CT) and unified case (fusion), in which case, information coming from both modalities are utilized. Both three dimensions (3D) and two dimensions (2D) versions of the algorithms were testes. Moreover, a simulation study is designed to obtain the best segmentation parameters. Finally, evaluation results of both methods are presented on patient data.

1.5 Organization of the thesis

The work organization is as follows. In Chapter 2, The methods to segment muscles are presented: First, basic level set methodology, terminology and numerical solutions of the equations are discussed widely. Then the unified model and proposed level set segmentation model is explained. Second, the other proposed segmentation model Bayesian Markov Random Field with partial volume model is explained. Chapter 3 explains how and why simulation study is designed and Ground Truth data are created. In Chapter 4, results and statistical evaluation of two models are presented. The last chapter, Chapter 5, includes the conclusions and future work.

CHAPTER 2

LEVEL SET AND BAYESIAN MARKOV RANDOM FIELD SEGMENTATION

2.1 Level Set Segmentation

The idea of curve evolution and evolving fronts or active contours were first introduced in [25] with the name Deformable Snakes. The main idea is that: A curve evolves in a way that it minimizes an energy function which depends on curve's external and/or internal properties. The model is based on a partial differential equation which is solved using Lagrangian framework. Later Osher and Sethian [26] defined the curve as the zero level set of an implicit hyper-surface. This is the first time Euler-Lagrange framework was introduced for curve evolution. This theory [26] is called Level Set theory. They used Hamilton-Jacobi methods (which is stable and convergent) to solve the Euler-Lagrange equation numerically. This approach increased the power of numerical solutions. Because Level Set model handles topological changes without extra effort as opposed to the Lagrangian solution in [25]. In Level Set Method, there is no need to track the front point by point, merging and splitting operations are made implicitly which gives the chance to handle topological changes easily even the topology is complex. Another advantage is, unlike Lagrangian method, increasing dimension of the model is straightforward.

The formal definition of level set method given in [26] is provided in Appendix B. The well known Level Set Equation is:

$$\phi_t + F|\nabla\phi| = 0. \tag{2.1}$$

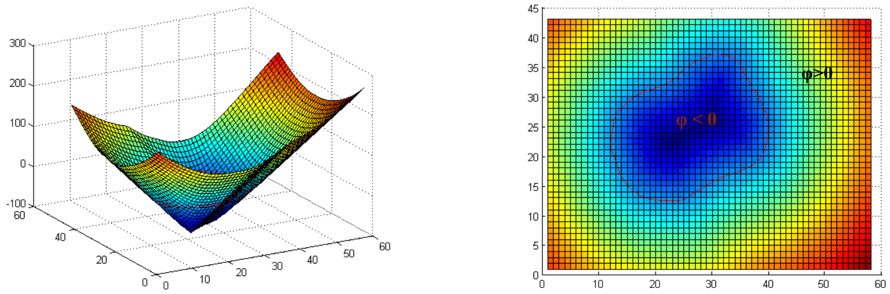

(a) (b)

Figure 2.1: Implicit Surface (ϕ) and its zero level set shown by red contour. (a) Side view (b) Upper view (Projection to the x-y plane)

Here ϕ is the implicit function whose zero level set is a curve defined as C. The implicit function is defined as a function of C such that ϕ is a signed distance function. Every point in the grid takes the value of its distance to the curve C. If a point is inside the curve, it takes a negative value and vice versa. If a point is on the curve (C), then it takes the value of zero. An example curve C (the red curve) and its distance function ϕ (conical shape in 3D) is illustrated ind Figure 2.1. In the illustration, the curve C is in two dimensions and the corresponding implicit function is three dimensional. The Level Set method carries the problem to higher dimension, as depicted in 2.1. Now many different closed curves in 2D are defined as zero level sets of one implicit function (ϕ) in 3D. As the curves evolve in time (under the effect of speed function F), splitting and merging of boundaries may happen, with level set method, these changes are implicitly handled. This very important result is one of the aspects that makes Level Set method powerful.

Signed distance function is Lipschitz continuous everywhere, except in the center of the curve (but it does not have a negative affect in practical application). It is differentiable everywhere, also near the boundary (C). These properties makes signed distance function an appropriate selection for the partial differential equations.

The level set equation comes with its nice properties, yet the numerical solution should keep these nice properties. The numerical solution to the level set equation has to be both stable and convergent. Stability refers to numerical solutions handle numerical errors such that numerical errors are not being accumulated in time. Convergency means that the steady state solution is reachable in finite time steps. In the next section, a numerically stable and convergent Level Set solution will be provided. Instead of Equation 2.1, the *convection* form of the Level Set Equation (Equation 2.3) (the motion in externally generated field) will be discussed, because these two equations can be derived from each other (Appendix B) and the numerical solution to the motion in externally generated field is more comprehensible.

2.1.1 Motion in an Externally Generated Velocity Field

Assume that there is a boundary defined by zero level set of implicit function (ϕ), $\phi(x) = 0$ and a velocity field, $\vec{V}(\vec{x})$ in 3D, $\vec{x}$ where $\vec{V} = \langle u, v, w \rangle$. The simplest method to move all the points according to this velocity field is solving

$$\frac{d\vec{x}}{dt} = \vec{V}(\vec{x}) \tag{2.2}$$

for every point $\vec{x}$. The front of the curve has to be discretized, but there are infinitely many points in the front. In every time step, it has to be discretized again to provide a correct numerical solution. In 2D, segments and in 3D, triangles can be used for discretizing [27]. This is not an issue if the front holds its connectivity. But even under the simplest velocity field large distortions forms, so front should be regularized and smoothed [26]. The topology changes are hard to handle. This equation is Lagrangian formulation. This Lagrangian formulation with regularizing, smoothing and surgical operations are called *front tracking methods*. Points for 2D and triangles for 3D has to be used as mentioned in [27]. Deformable Model [25] is a front tracking method as stated in the beginning part of this chapter. Instead of Lagrangian formulation the Level Set formulation,

$$\phi_t + \vec{V} \cdot \nabla\phi = 0, \tag{2.3}$$

which enjoys the properties of *Hamilton-Jacobi Equations* is in the scope of this study. In the Equation ϕ_t is time derivative of the implicit function and $\nabla\phi = \langle \phi_x, \phi_y, \phi_z \rangle$. If gradient operator is written in open form we have

$$\vec{V} \cdot \nabla\phi = u\phi_x + v\phi_y + w\phi_z. \tag{2.4}$$

This type of Level Set equation (Equation 2.3) where there is an external vector field ($\vec{V}$) is also used in combustion reaction model. For combustion reaction $\phi = 0$ represents the surface of reaction of a moving flame front [27]. This equation is sometimes called *convection* equation. In this study it is also referred as *convection* equation. Numerical solution of the Equation 2.3 will be given in following sections.

2.1.1.1 Discretization of Convection Equation and Upwind Differencing Methods

The discretization of the Equation 2.3 in time could be done with *forward euler time* or *backward euler time*. Discretization using the latter will be given in 2.1.4. Now *Forward Euler Time* is the one to be focused at: At time t we have the values $\phi^n = \phi(t^n)$ and at $t^{n+1} = t^n + \Delta t$ we have $\phi(t^{n+1})$. Then discretizing in time with forward euler step is

$$\phi_t = \frac{\phi^{n+1} - \phi^n}{\Delta t}. \tag{2.5}$$

Write this in Equation 2.3 to obtain,

$$\frac{\phi^{n+1} - \phi^n}{\Delta t} + \vec{V}^n \cdot \nabla\phi^n = 0. \tag{2.6}$$

Spatial derivatives: One can evaluate spatial derivatives using this straightforward approach used for time derivation, but it does not give a stable solution. More effort is needed, So we start by writing the Equation 2.3 in expanded form in 3D,

$$\frac{\phi^{n+1} - \phi^n}{\Delta t} + u\phi_x + v\phi_y + w\phi_z = 0. \tag{2.7}$$

This equation can be discretized in dimension by dimension manner. For the sake of simplicity, the equation is now only for one dimension x and for a specific grid location i and written,

$$\frac{\phi_i^{n+1} - \phi_i^n}{\Delta t} + u_i^n(\phi_x)_i^n = 0, \tag{2.8}$$

where ϕ_i^n is the spatial derivative of ϕ at the point x_i. When $u_i > 0$, the values of ϕ or the information is moving from left to right. Method of characteristics tells to take the spatial information from left to calculate which value of ϕ will take place on x_i. Then a first order scheme

$$\frac{\partial\phi}{\partial x} = \frac{\phi_i - \phi_{i-1}}{\Delta x} \tag{2.9}$$

for $u_i > 0$ is written. This is a first order accurate *backward difference* spatial discretization operation and symbolized as $D^-\phi$ (where $D^-\phi$ is the backward difference operator). If $u_i < 0$, the values of ϕ now are moving from right to left and we should take the spatial information from right of the point x_i, then this scheme

$$\frac{\partial\phi}{\partial x} = \frac{\phi_{i+1} - \phi_i}{\Delta x} \tag{2.10}$$

is used. Similar to the backward difference scheme, this is first order accurate *forward difference* and operation is symbolized as $D^+\phi$ (where $D^+\phi$ is the forward difference operator). Using the spatial information in the direction opposite to the moving direction of the values of ϕ is called *upwinding* [27]. Verbally spoken, when u is positive, vector field has a component heading to right, the value of the implicit function and information moves right. Upwinding method takes the spatial information from left and vice versa when u is negative.

2.1.1.2 Hamilton-Jacobi Essentially Non-Oscillatory Schemes

The upwinding methods introduced in the previous section can be improved to have better approximation. In this manner the number of points to calculate the numerical spatial derivative. A good approximation should be smooth and represent data well. Hamilton-Jacobi Essentially Non-Oscillatory (HJ ENO) are designed [28], [29] based on these two aspects. These schemes are 1st, 2nd, 3rd and 5th order. The first three are given in Appendix C. But to summarize the first one it is the first order upwinding scheme described in Section 2.1.1.1. The second and third order approximation uses second and third order derivative approximations respectively. For these higher order terms scheme selects the direction which gives a smaller change in the function. Taking information from less smooth direction is not desired. With this choice higher order derivatives do not create oscillations. For every grid point and for every time step schemes select one of two stencils: right biased or left biased. In HJ Weighted Non-Oscillatory Scheme (HJ WENO) instead using this selection criteria a weighted interpolation of these four stencils are used. Weights change according to their smoothness and smoothness is measured using Equations 2.15,2.16 and 2.17. Following paragraphs gives the procedure in detail.

For the approximation of $\phi^-_{x_i}$ the third order HJ ENO uses subset of the left biased stencil $\{\phi_{i-3}, \phi_{i-2}, \phi_{i-1}, \phi_i, \phi_{i+1}, \phi_{i+2}\}$. As in [30] the subset stencils are $\{\phi_{i-3}, \phi_{i-2}, \phi_{i-1}, \phi_i\}$, $\{\phi_{i-2}, \phi_{i-1}, \phi_i, \phi_{i+1}\}$ and $\{\phi_{i-1}, \phi_i, \phi_{i+1}, \phi_{i+2}\}$ (see Figure 2.2).

Let's define $v_1 = D^-\phi_{i-2}$, $v_2 = D^-\phi_{i-1}$, $v_3 = D^-\phi_i$, $v_4 = D^-\phi_{i+1}$ and $v_5 = D^-\phi_{i+2}$ as defined in [27]. Where D's are differencing operator as defined in Section 2.1.1.1. Then three possible $\phi^-_{x_i}$ are

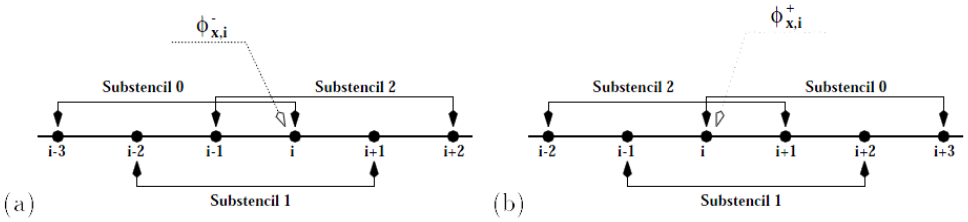

Figure 2.2: Three subsets of the stencil: (a) Left biased stencil to calculate $\phi^-_{x_i}$ (b) Right biased stencil to calculate $\phi^+_{x_i}$ [30].

$$\phi^1_x = \frac{v_1}{3} - \frac{7v_2}{6} + \frac{11v_3}{6} \tag{2.11}$$

$$\phi^2_x = -\frac{v_2}{6} - \frac{5v_3}{6} + \frac{v_4}{3} \tag{2.12}$$

and

$$\phi^3_x = -\frac{v_3}{3} + \frac{5v_4}{6} - \frac{v_5}{6} \tag{2.13}$$

Proceeding in the lines of [27] it is seen that in [28] it was proposed to use a convex combination of three possible 3rd order difference schemes to obtain a smooth interpolation of the data and they called the method WENO (Weighted ENO). The weights are chosen in such a way that finite difference calculated next to a discontinuity is given the value of zero. In smooth regions, all three approximations equally effects the interpolation. After, in [29] Jiang et. al. calculated optimal weights. They obtained 5^{th} order accuracy in smooth regions. Later [30] modified the WENO and adapted in to the HJ framework. Now in the following paragraphs the HJ WENO will be explained. The weighted polynomial is given

$$\phi_x = \omega_1\phi^1_x + \omega_2\phi^2 + \omega_3\phi^3 \tag{2.14}$$

where $0 < \omega_k \leqslant 1$ and $\omega_1 + \omega_2 + \omega_3 = 1$. This equation is convex combination of ω_1,ω_1 and ω_3 which were given in equations (2.11), (2.12) and 2.13. The optimal weights for smooth regions are $\omega = 0.1$, $\omega = 0.6$ and $\omega = 0.3$. But in non smooth regions only one of the stencils is used to provide backward difference, $\omega_k = 1$ and the other weights are 0. In [30] in order to define weights they have used smoothness metrics of stencils such as

$$S_1 = \frac{13}{12}(v_1 - 2v_2 + v_3)^2 + \frac{1}{4}(v_1 - 4v_2 + 3v_3)^2, \tag{2.15}$$

$$S_2 = \frac{13}{12}(v_2 - 2v_3 + v_4)^2 + \frac{1}{4}(v_2 - v_2)^2 \tag{2.16}$$

and

$$S_3 = \frac{13}{12}(v_3 - 2v_4 + v_5)^2 + \frac{1}{4}(3v_{-}4v_3 + v_5)^2. \tag{2.17}$$

Then new variables which depend on these smoothness measures are given,

$$\alpha_1 = \frac{0.1}{S_1 + \epsilon} \tag{2.18}$$

$$\alpha_2 = \frac{0.6}{S_2 + \epsilon}, \tag{2.19}$$

and

$$\alpha_3 = \frac{0.3}{S_3 + \epsilon}. \tag{2.20}$$

If a region is smooth, corresponding α value becomes large. ϵ is scale factor suggested in [31] and is defines as,

$$\epsilon = 10^{-6}\{v_1^2, v_2^2, v_3^2, v_4^2, v_5^2\} + 10^{-6} \tag{2.21}$$

.

In smooth regions, S_k's goes to 0 and when they are negligibly small comparing to ϵ then coefficients become. $\alpha_1 \approx 0.1\epsilon^2$,$\alpha_2 \approx 0.6\epsilon^2$ and $\alpha_3 \approx 0.3\epsilon^2$. The a_k's are normalized to obtain weights

$$\omega_1 = \frac{\alpha_1}{\alpha_1 + \alpha_2 + \alpha_3}, \tag{2.22}$$

$$\omega_2 = \frac{\alpha_2}{\alpha_1 + \alpha_2 + \alpha_3} \tag{2.23}$$

and

$$\omega_3 = \frac{\alpha_3}{\alpha_1 + \alpha_2 + \alpha_3}. \tag{2.24}$$

and if we continue the calculation in a smooth region, $\omega_1 = \frac{0.1\epsilon^2}{0.1\epsilon^2 + 0.6\epsilon^2 + 0.3\epsilon^2} = 0.1$ and similarly $\omega_2 = 0.6$, $\omega_3 = 0.1$. For example, if one of the stencils are discontinuous , related S_k will be large and related coefficient ω will be a small value and will have a little contribution to the final approximation. If two of them have discontinuities then related coefficient will be small and the other will dominate. The last condition where each three stencils have discontinuities is a difficult case for HJ ENO and is very rare and the problem is alleviated in time.

Here only approximation of ϕ_x^- is given, similar procedure should be followed for ϕ_x^+ in right biased stencil (Figure 2.2).

2.1.1.3 Convergency and Stability

The Lax-Richtmayer equivalence theorem says that a finite difference approximation to a linear partial differentiation is convergent (the solution is correct when $\Delta t \rightarrow 0$ and $\Delta x \rightarrow 0$) if the solution is consistent and stable. The discretizing with upwinding and forward euler is consistent because the approximation error is 0 when $\Delta t \rightarrow 0$ and $\Delta x \rightarrow 0$.

Stability means that small roundoff errors in the numerical scheme does not grow in time. Stability can be obtained by Courant-Freidreichs-Lewy (CFL) condition. This condition says numerical waves should propagate faster than the physical vector field. The CFL time step restriction is,

$$\Delta t < \frac{\Delta x}{max\{|u|\}}. \tag{2.25}$$

Here $max\{|u|\}$ is the maximum speed of the numerical wave. And to determine time step (Δt) which makes the solution stable, a parameter is introduced such as,

$$\Delta t \frac{max\{|u|\}}{\Delta x} = \alpha \tag{2.26}$$

and $0 < \alpha < 1$. In 3D CFL restriction can be written as

$$\Delta t max\{\frac{|u|}{\Delta x} + \frac{|v|}{\Delta y} + \frac{|w|}{\Delta z}\} = \alpha \tag{2.27}$$

or,

$$\Delta t \frac{max|\vec{V}|}{min\{\Delta x, \Delta y, \Delta z\}} == \alpha. \tag{2.28}$$

$|\vec{V}|$ is magnitude of the velocity field such as

$$|\vec{V}| = \sqrt{u^2 + v^2 + w^2}. \tag{2.29}$$

In our problem $\Delta x = \Delta y = \Delta z = 1$ and does never change so to provide stability in every iteration time step has to be calculated according to Equation 2.27 or alternatively Equation 2.28.

2.1.2 Hamilton-Jacobi Equations

In this section, a general solution method of Hamilton-Jacobi equations of the form

$$\phi_t + H(\nabla\phi) = 0 \tag{2.30}$$

will be discussed. Convection Equation 2.3 and level set Equation 2.1 are Hamilton-Jacobi equations. This generalization is last step to give a numerical solution to the standard level set solution. In following paragraphs the methods applied to solve convection equation is generalized by examining Hamilton-Jacobi equation, The HJ equation in three dimensions is

$$\phi_t + H(\phi_x, \phi_y, \phi_z) = 0. \tag{2.31}$$

$H(\phi_x, \phi_y, \phi_z) = \vec{V} \cdot \nabla\phi$. The numerical discretization in time using Forward Euler time gives

$$\frac{\phi^{n+1} - \phi^n}{\Delta t} + \hat{H}(\phi_x^-, \phi_x^+; \phi_y^-, \phi_y^+; \phi_z^-, \phi_z^+) \tag{2.32}$$

where $\hat{H}(\phi_x^-, \phi_x^+, \phi_y^-, \phi_y^+, \phi_z^-, \phi_z^+)$ is the discrete Hamiltonian. If $|H_1| = \frac{\partial H}{\partial \phi_x}$,$|H_2| = \frac{\partial H}{\partial \phi_y}$ and $|H_3| = \frac{\partial H}{\partial \phi_z}$ is define the CFL time step restriction as stated in Section 2.1.1.3 is

$$\Delta t max \left\{ \frac{|H_1|}{\Delta x} + \frac{|H_2|}{\Delta y} + \frac{|H_3|}{\Delta z} \right\} < 1 \tag{2.33}$$

The Hamiltonian for Convection Equation (Equation 2.3) is $H(\phi_x, \phi_y, \phi_z) = u\phi_x + v\phi_y + w\phi_y$.

Note that numerical Hamiltonian $\hat{H}$ is the function of backward $(\phi_x^-, \phi_y^-, \phi_z^-)$ and forward $(\phi_x^+, \phi_y^+, \phi_z^+)$ differences. These difference can be calculated with HJ ENO or HJ WENO schemes. For every dimension there are two options: ϕ_x^+ ϕ_x^-. To obtain the numerical correct solution the right one has to be chose.The following numerical method is to tell which one is a better choice. This method is called Godunov's scheme, in two dimensions it is:

$$\hat{H} = \text{ext}_x \text{ext}_y H(\phi_x, \phi_y) \tag{2.34}$$

Here ext_x is defined as: if $\phi_x^- > \phi_x^+$ then H takes the minimum value in the interval where $I\phi_x \in \{\phi_x^-, \phi_x^+\}$ and if $\phi_x^- < \phi_x^+$ H takes the maximum value in the interval. For y and z same procedure can be followed. In applications the order of ext_x,ext_y and ext_z effects the solution, but in our problem this will not change the solution since $\text{ext}_x\text{ext}_y H = \text{ext}_x\text{ext}_y H$. There are six possibilities for 3D but they are all equal again for our problem.

Let's get back to the convection (Equation 2.3) to see its numerical solution by Godunov's scheme. Hamiltonian H is separable: $\text{ext}_x\text{ext}_y H(\phi_x, \phi_y) = ext_x(u\phi_x) + ext_y(v\phi_y)$. In the case, where $\phi_x^- < \phi_x^+$,the minimum value of $u\phi_x$ should be chosen according to Godunov's Scheme and this choice depends on the sign of u. If u is positive ($u > 0$), $u\phi_x^-$ is selected and if u is negative ($u < 0$), $u\phi_x^+$ is selected. Similarly when $\phi_x^- > \phi_x^+$ the maximum is picked by the scheme: The scheme chooses maximum possible value of $u\phi_x^-$ and it depends on the sign of u. If it is negative ($u < 0$), the scheme chooses $u\phi_x^+$; else the scheme chooses $u\phi_x^-$. When $u = 0$ the choice is trivial. To summarize these operations , scheme says: If $u < 0$ use ϕ_x^+; if $u > 0$,use ϕ_x^- and if $u = 0$, the result is regardless of the choice. In conclusion, Godunov scheme for convection equation is simple upwinding scheme described in Section (2.1.1.1) for the Equation 2.3.

Godunov scheme is not only the scheme to solve Hamilton-Jacobi equations. Schemes like Roe-Fix Scheme,and Lax-Friedrichs schemes can be used also. In this study Godunov Scheme is used, because it is easy to implement and gives sufficiently good results.

2.1.3 Motion in Normal Direction

The equation of motion in normal direction is the general Level Set Equation 2.1. Let's rewrite it:

$$\phi_t + F|\nabla\phi| = 0. \tag{2.35}$$

As stated earlier, it is a Hamilton-Jacobi equation and the numerical methods are mentioned in Section 2.1.1. In Hamilton-Jacobi model solutions, we need H_1, H_2 and H_3 which are the partial derivatives of the Hamiltonian (H) with respect to ϕ_x, ϕ_y, and ϕ_z respectively in 3D. Here in Equation 2.35, $H = F|\nabla\phi|$. Note that, $|\nabla\phi| = \sqrt{\phi_x^2 + \phi_y^2 + \phi_z^2}$ then

$$H_1 = F\frac{\partial H}{\partial \phi_x} = F\frac{2\phi_x}{2|\nabla\phi|} = F\frac{\phi_x}{|\nabla\phi|}. \tag{2.36}$$

Similarly,

$$H_2 = F\frac{\phi_y}{|\nabla\phi|} \tag{2.37}$$

$$H_3 = F\frac{\phi_z}{|\nabla\phi|} \tag{2.38}$$

can be written following the steps to find H_1. If we write the equation convection form,

$$\phi_t + \left(F\frac{\phi_x}{|\nabla\phi|} + F\frac{\phi_y}{|\nabla\phi|} + F\frac{\phi_z}{|\nabla\phi|}\right) \cdot \nabla\phi = 0 \tag{2.39}$$

it is easier to compare Equation 2.3 with Equation 2.35. Recall that in motion by externally generated field (Equation 2.3) $\vec{V} = \langle u, v, w \rangle$ and here we have $\langle u, v, w \rangle = \langle H_1, H_2, H_3 \rangle$. The connection between convection Equation 2.3 and 2.35 is clear now. All methods prescribed before are all applicable.

The time step restriction can be found using Equation 2.33 by plugging the values of H_1, H_2 and H_3.

For spatial discretization of this type of equation as stated earlier Godunov scheme is used. In Table 2.1 the method is summarized. Where $\phi_x^- < 0$ and $\phi_x^+ > 0$ (*V-shaped* expansion region) two partial derivatives have different signs. In expansion characteristics of the equation data is in both direction and outwards. Godunov scheme minimizes H (since $\phi_x^+ > \phi_x^-$) by choosing the $\phi_x = 0$. In an an expansion region function should be locally smooth [27]. Godunov provides this without adding artificial dissipation (second order partial derivatives). Godunov avoids the error introduced by artificial dissipation. At grid points where $\phi_x^- > 0$ and $\phi_x^+ < 0$, the information is coming from both sides causing shock. Godunov maximizes H (since $\phi_x^- > \phi_x^+$)by choosing the fastest of derivatives reaching that point. Then maximization ends up with choosing the larger of ϕ_x in magnitude. Again problem is circumvented without artificial dissipation. The other cases are simple upwinding discussed before.

Table 2.1: The spatial derivative choices of Godunov Scheme, ϕ is the level set function and subscripts x and y are to represent partial derivatives. F is a scalar on the coordinates (x, y)

	$\phi^-, \phi^+ > 0$		$\phi^-, \phi^+ > 0$			
	$\phi^- < \phi^+$	$\phi^- > \phi^+$	$\phi^- < \phi^+$	$\phi^- > \phi^+$	$\phi^+ > 0, \phi^- < 0$	$\phi^+ < 0, \phi^- > 0$
$F > 0$	ϕ_x^-	ϕ_x^-	ϕ_x^+	ϕ_x^+	$\phi_x = 0$	$max\{\lvert\phi_x^-\rvert, \lvert\phi_x^+\rvert\}$
$F < 0$	ϕ_x^+	ϕ_x^+	ϕ_x^-	ϕ_x^-	$\phi_x = 0$	$min\{\lvert\phi_x^-\rvert, \lvert\phi_x^+\rvert\}$

2.1.4 Curvature Evolution

Curvature evolution is an important aspect in curve evolution methods. In our solution method, curvature evolution is important. In curvature evolution, curve moves under effect of its curvature. It is different from convection since movement depends on the internal properties of the curve. The points with higher curvature will move faster. So the curve becomes much smoother until it becomes a circle. Finally, it collapses i.e. shrinks to a point.

Here in this section, numerical methods will be given to solve the equation. Only shrinking evolution is discussed and is used in algorithms since curvature growing is an ill-posed problem and error increases in time leading wrong solutions.

Recall the Equation 2.1,

$$\phi_t + F|\nabla\phi| = 0. \tag{2.40}$$

Now set $F = -b\kappa$ where b is constant and greater than zero and κ is the mean curvature of the implicit function (ϕ). Definition and derivation of mean curvature for 2D and 3D is given in Appendix D.

When F plugged into the Equation 2.1

$$\phi_t = b\kappa|\nabla\phi|. \tag{2.41}$$

is obtained. In the curve evolution on the coordinates where the shape is convex, mean curvature will be positive and the points will propagate inwards and in concave regions mean curvature will be negative resulting in the motion outwards. In Figure 2.3 the signs of curvatures are illustrated and in Figure 2.4 an example of mean curvature evolution is illustrated. In the figure it is easy to see the direction of motion is outwards in concave and inwards in convex regions. Also note that the amount of propagation is larger in the regions where the curvature is large in magnitude. Hence the shape shrinks and before collapsing it takes a round form (which is a circle in 2D and sphere in 3D).

Forward time step is an appropriate solution, but since the right side depends on curvature (so on second derivatives of the implicit function ϕ), the equation is parabolic and not hyperbolic. Therefore upwinding methods used for advection Equation 2.3 cannot be used. The information does not come from only one direction, rather is coming from both directions. As a result, central difference scheme for spatial derivative is appropriate. Remembering that central difference approximation is:

$$\phi_x = \frac{\phi_{i+1} - \phi_{i-1}}{2\Delta x} \tag{2.42}$$

Then CFL time restriction is

$$\Delta t max\left\{\frac{2b}{(\Delta x)^2} + \frac{2b}{(\Delta y)^2} + \frac{2b}{(\Delta z)^2}\right\} < 1. \tag{2.43}$$

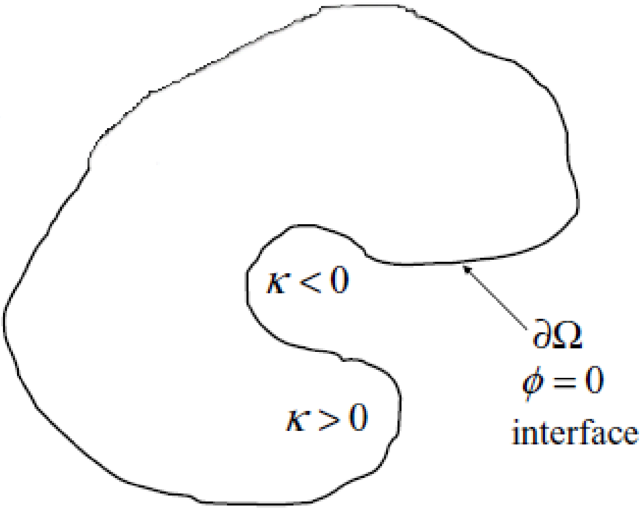

Figure 2.3: Curvature directions on the boundary [27].

It restricts the time step a lot because denominator is now squared. Making time step smaller loads a high burden to the numerical solution. It decreases the time step (δt) more and increases the number of steps until convergence. Another numerical method which does not bring any restriction to time step selection is Backward Euler Method. The mathematical details as in [20] is given in Appendix E.

2.2 Geometric Integral Measures

Until here in this Chapter, numerical methods to solve level set equations were given. But nothing about the scalar field F in Equation 2.1 was discussed. F determines the motion of the curve. In this section mathematical background of deriving scalar function F from energy functionals $E(C)$ that depends on the evolving curve C is given. These energy functionals are integrals over a region (enclosed or disclosed by C) or closed contour integrals on the boundary (C). The level set solution will find the curve C which minimizes the integral. The general variational procedure to obtain speed terms (F) minimizing an energy integral can be summarized as this:

(i) The energy functional $E(C)$ is defined, (ii) The first variation $\frac{\delta E}{\delta C}$ is calculated. The result is

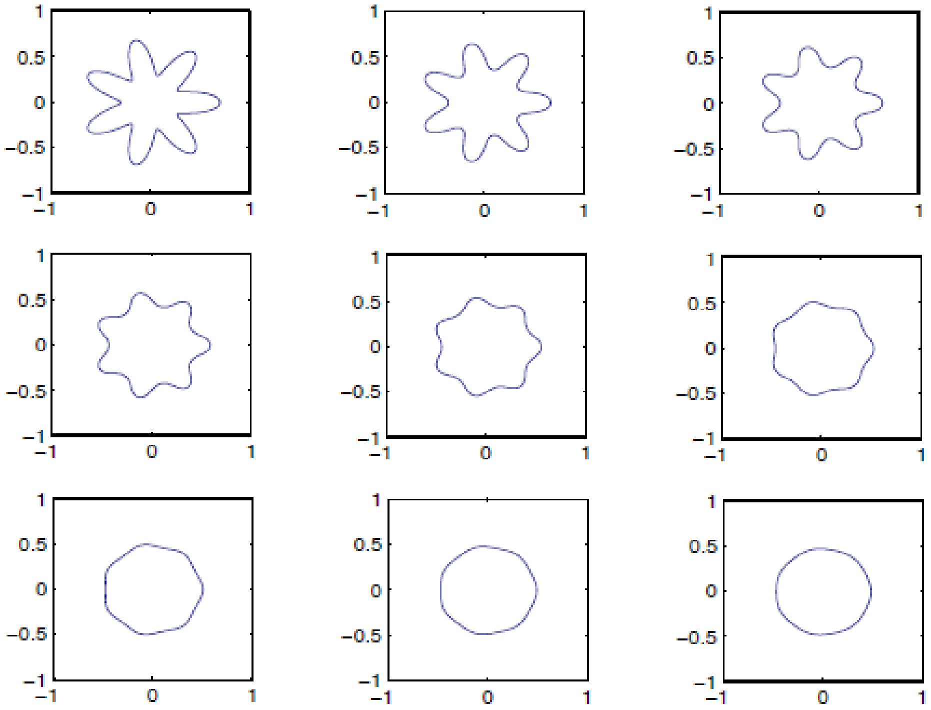

Figure 2.4: Curvature motion of a star shaped curve [27].

the curve evolution equation $C_t = -\frac{\delta E}{\delta C}$ where C_t is velocity of the curve. (iii) Speed function F is related a s$C_t = \mathbf{n}$. Finally we plug speed function F into the level set Equation 2.1.

In the next two Sections (2.2.1 and 2.2.2), this procedure will be applied and the segmentation model is described.

2.2.1 Geodesic Active Contours, Surfaces

This term was first introduced in [18] and explained using variational framework. In this section, we will follow the derivation which was given in the study. First, let's examine a general contour integral measure in 2D. Where g is a scalar function.

$$E(C) = \oint_C g(C(s))\, ds. \tag{2.44}$$

After taking first variation and arrange it in the level set form (see Appendix E) the equation

$$\phi_t = (\kappa g - \langle \nabla g . \frac{\nabla \phi}{|\nabla \phi|} \rangle)|\nabla \phi| \tag{2.45a}$$

$$\phi_t = \kappa g |\nabla \phi| - \langle \nabla g, \nabla \phi \rangle |\nabla \phi|. \tag{2.45b}$$

is obtained. Notice that if g is chosen to be 1 everywhere, then we have

$$\phi_t = b\kappa |\nabla \phi|. \tag{2.46}$$

It is the Equation 2.41, motion of a curve shrinking under its own curvature as given in previous Section 2.1.4. In our segmentation model we need smoothing but also we need to preserve sharp structures like thin muscles. The Edge indicator is a stopping function:

$$g(I) = \frac{1}{1 + |\nabla G_\sigma * I|^2} \tag{2.47}$$

where G is gaussian with variance σ. The denominator is smoothed image gradient. for 2D it is $G_x^2 + G_y^2$ and in 3D it is $G_z^2 + G_y^2 + G_z^2$. The G_x, G_y and G_z are smoothed image gradients in x,y,z directions respectively. g becomes small when the gradient is large as illustrated in Figure 2.5. It is positive everywhere. It was previously used in the model called geometric active contour model [16]:

$$\phi_t = g(I) div \left(\frac{\nabla \phi}{|\nabla \phi|} \right) + c g(I) |\nabla \phi|. \tag{2.48}$$

This model is similar to Geodesic Active Contours (GAC) model introduced in Equation 2.45b but second term is different. Here g is used as balloon force (or weighted area term). The curve evolution stops where the gradient is large and g is 0. But only in the perfect edges g takes the value 0. In real images especially in medical data because of noise there are many zeros that are not edges. In these regions this model stops. Also one drawback is that this term is positive everywhere, meaning that curves evolves in one direction so the result depends more on the initialization.

In the new GAC model, instead of second term, there exists $\langle \nabla g, \nabla \phi \rangle$ which drags level set to the valleys of function g (Figure 2.5). In addition, the balloon force (as in earlier proposed model i.e. Geometric model [18]) can be added to the model to make iterations converge faster. Then the whole model is achieved:

$$C_t = (-cg - \kappa g + \langle \nabla g . \mathbf{n} \rangle)\, \mathbf{n} \tag{2.49}$$

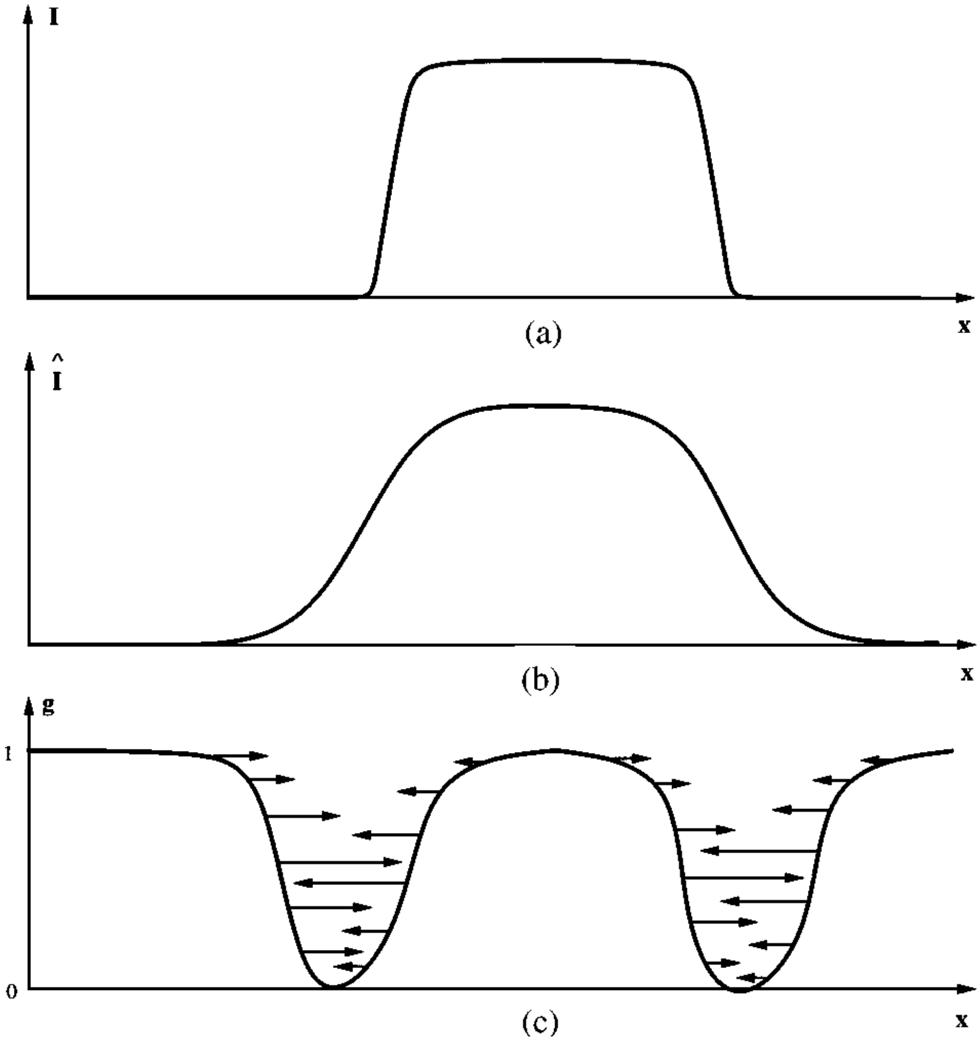

Figure 2.5: 1D illustration of the GAC model, (a) I vs x, An edge in an image(I) (b) $\nabla G_{\sigma} * I$ vs x, smoothed version of (a). (c) Edge indicator function g and directions of the curve through the valleys [18].

where c is a scalar. Now the model is named *Geodesic* rather than *Geometric*. In this study, balloon force term is dropped since we need accuracy rather than speed.

2.2.2 Minimum Variance

It is an energy term based on the Mumford-Shah model [14]. Chan and Vese approximated and solved this functional efficiently by using Level Set methods in [15]. The derivations again will be given for 2D (contours) for the sake of simplicity. The 3D extension is straightforward and trivial. Minimal variance energy functional is:

$$E = \frac{1}{2}\int\int_{\Omega_C}(I - c_1)^2 dxdy + \int\int_{\Omega/\Omega_C}(I - c_2)^2 dxdy \tag{2.50}$$

Minimizing this functional means to find the curve C separating space into two smooth regions (i.e. variances of inner and outer regions are small). This is why this term is called minimum variance term. The corresponding level set equation is:

$$\phi_t + (c_1 - c_2)\left(I - \frac{c_1 + c_2}{2}\right)|\nabla\phi| = 0. \tag{2.51}$$

where c_1 and c_2 are average values (see Appendix F for the full derivation) of inner and outer regions. In the evolution process, boundary avoids from the background mean c_2 and trying to be close to the mean c_1. Every step c_1 and c_2 are supposed to become closer to the real mean of the regions that we are trying to segment. As can be seen easily, Equation F.17 becomes zero at places where $I = \frac{c_1+c_2}{2}$, negative if $I < \frac{c_1+c_2}{2}$ and positive when $I > \frac{c_1+c_2}{2}$. This means the curve will shrink in the background region where $I > \frac{c_1+c_2}{2}$, will expand in the desired region where $I < \frac{c_1+c_2}{2}$ and will stop in the boundary where $I = \frac{c_1+c_2}{2}$.

In [15] the reason why they call the model active contours without edges is that curve does not need the edge information as geodesic active contour do so. As a result, this terms works well in noisy data case because, if the noise has zero mean, it does not effect the mean intensity values of the classes.

2.3 Level Set Segmentation Model

Here in this section, the Level Set segmentation model used to segment muscles is described. The Level Set segmentation model used in this study is a binary segmentation model i.e. it separates foreground from background. The objective is to segment face muscles but in human head data there are several tissue types. These are mainly skin, veins, glands, muscles, fat, bone (skull and teeth), marrow and air. In CT and MRI, glands, muscles and veins have similar intensity values so in this study they are considered as same class and called **Muscle** class. The marrow is inside the bone and resides in the cavities of the bone, so marrow, teeth and skull are considered as same class and named **Bone** class. The skin tissue has intensity values similar to Muscle class but treated as a different class. It is not possible to segment these classes using one binary segmentation step. It is possible to do hierarchical level set segmentation to segment more than two classes [20] but here, in this thesis other classes are segmented using simpler image processing techniques. There are two main reasons: Firstly Level Set method is a computationally expensive method and secondly, (mimic muscle segmentation is the main focus of this study) there is no need for high accuracy segmentation for classes other than Muscle. These simple image processing methods will be called preprocess and postprocess steps of the model. Level Set segmentation process is compromised of three parts: (i) preprocess, (ii) solving level set equation (main part) and (iii) finally postprocess. The complete model is provided in Figure 2.6.

The objective of the Preprocess step is to remove Air and Bone classes from images and then to provide initial segmentations using K-means method (Section 2.3.1). Main Part does the actual segmentation using Level Set segmentation methodology (Section 2.3.2). Post Process has two parts: The first part is optional which will be explained in Section 2.3.3.

2.3.1 Preprocess

Preprocess has two main goals the first is to eliminate tissues that is not in the focus of this study. These classes are Bone and Air and these two classes have the respectively highest and lowest mean intensity value in CT image. So applying two thresholds (172 HU for upper and -609 HU for lower threshold) on CT data Air and Bone can easily be removed and is used as a binary mask: In the regions of interest (Muscle and Fat) *Mask* takes the value of 1 otherwise 0. In the Main segmentation part only the information where mask is nonzero is used. The marrow tissue resembles muscles so in this thresholding process the marrow tissues is not removed. But it is known that marrow is inside bone. Therefore if the bone is filled using binary flood fill operation the marrow is also removed and this completes the mask and first part of Preprocess.

The second part's aim is to provide a initial segmentation to help level set algorithm converge faster and prevents it from getting stuck in local minima. The K-means algorithm is used for this purpose. The K-means algorithm is a basic iterative clustering algorithm and it finds predefined number of classes and classifies voxels based on their distances to cluster means. In this part, the image is separated into two regions foreground (initial Muscle class) and background (initial Fat class). Then the signed distance function is calculated such that muscle class takes negative values and vice versa. Preprocess part completes its work here and provides an initial segmentation for the Level Set algorithm (the main part).

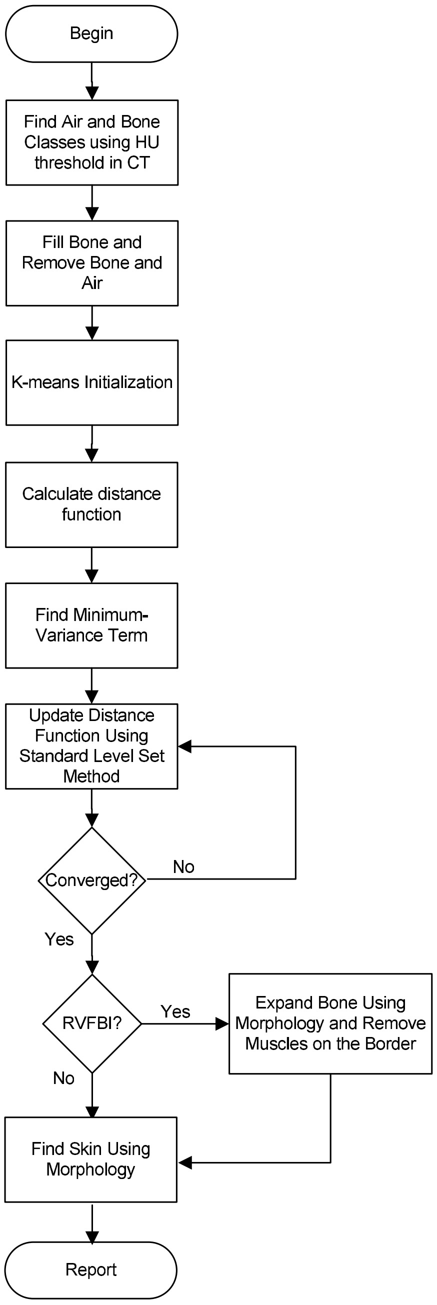

Figure 2.6: Standard Level Set (Forward Euler) Segmentation Method

2.3.2 Main Part

In Figure 2.6 blocks in between ‘K-means Initialization’ and ‘RVBFI’ forms main part of the standard Level Set model. The main part is the Level Set solution of the segmentation problem. It uses numerical methods and theory described before in previous sections. These methods are combined accordingly to obtain the main part. If geodesic term and minimum variance terms are weighted with scalars (α, β) and combined in one level set equation one obtains:

$$\phi_t = \left\{ \alpha \left(\kappa g - \langle \nabla g.\mathbf{n} \rangle \right) + \beta \left[(c_2 - c_1)(I - \frac{c_1 + c_2}{2}) \right] \right\} |\nabla \phi|. \tag{2.52}$$

This is the model for one type of modality (either MR or CT). It is possible to obtain better results if MRI and CT modality images are unified. In this case mean intensities (c_1 and c_2) and image intensity value I of each modality constitutes the *Minimum Variance* term:

$$F_{MV} = \gamma (c_2^{MR} - c_1^{MR}) \left(I^{MR} - \frac{c_1^{MR} + c_2^{MR}}{2} \right) + (1 - \gamma)\, (c_2^{CT} - c_1^{CT}) \left(I^{CT} - \frac{c_1^{CT} + c_2^{CT}}{2} \right) \tag{2.53}$$

where γ is the weighting factor and $\gamma \in [0, 1]$ which determines the effect of the modality to the equation. γ is the third parameter with α and β (all are positive scalars).

Similarly geodesic term is also modified for unified data. The stopping function g was modified to **metric tensor** G as in [32][33],

$$G = \sum_{b=1}^{M} \begin{bmatrix} I_x^2 & I_x I_y & I_x I_z \\ I_y I_x & I_y^2 & I_y I_z \\ I_z I_x & I_z I_y & I_z^2 \end{bmatrix} \tag{2.54}$$

where the elements of the matrix are partial derivatives of images, b is the number of bands (in our case $M = 2$: MRI and CT data). For an edge, the differences between maximum and minimum eigenvalue is large.Therefore edge indicator function for unified data was chosen as:

$$g(I) = \frac{1}{1 + (\lambda^+ - \lambda^-)} \tag{2.55}$$

Where (λ^+) is the maximum eigenvalue and (λ^-) is the minimum eigenvalue.

In the model, first term (the geodesic part) does the smoothing (diffusion) using edge information and second term (minimum variance term) is creates the discontinuity in the level set function and separates space in two regions. The model seeks for regions with uniform intensity inside and outside with smooth boundaries in between. The balance of two terms create the regions. Less smoothing may result in noisy boundaries while much smoothing may result in over smoothed boundaries or may cause the level set completely collapse to a point.

In Equation 2.52: The geodesic part has a curvature term that is parabolic and remaining parts are hyperbolic. Minimum variance term has only one solution option that is the Forward Euler solution. But for the parabolic part there are two options, Explicit Solution (Forward Euler Time) and Implicit Solution (Backward Euler Time) which were discussed in Section 2.1.4.

Explicit Model: For explicit solution, as in Section 2.1.3 hyperbolic terms H_1, H_2 and H_3 are defined as $H_1 = F_H\frac{\phi_x}{|\phi|}$, $H_2 = F_H\frac{\phi_y}{|\phi|}$ and $H_3 = F_H\frac{\phi_z}{|\phi|}$ where in our model $F_H = \alpha\langle\nabla g.\mathbf{n}\rangle + \beta\left[(c_1 - c_2)(I - \frac{c_1+c_2}{2})\right]$ is the hyperbolic part and $F_P = \kappa g$. So the CFL condition for hyperbolic terms (as described in Equation 2.33) and parabolic terms (Equation 2.43) are combined to write

$$\Delta t \max\left\{\frac{|H_1|}{\Delta x} + \frac{|H_2|}{\Delta y} + \frac{|H_3|}{\Delta z} + \frac{2g}{(\Delta x)^2} + \frac{2g}{(\Delta y)^2} + \frac{2g}{(\Delta z)^2}\right\} < 1. \tag{2.56}$$

CFL condition above gives the time step. So for one dimension update equation is

$$\phi^{n+1} = \phi^n + \Delta t(F|\nabla\phi^n_x|). \tag{2.57}$$

Spatial derivatives are found using Hamilton-Jacobi Essentially Non Oscillatory schemes in desired accuracy (one up to five order).

The Level Set segmentation algorithm is given in Figure 2.7.

θ is a positive scalar and a variable parameter, in every θ steps GAC model is applied otherwise only Chan-Vese model (only variance term) is used to update ϕ.

Implicit Model: For the implicit model in this study [19] is used. Here we evaluate implicit function ϕ^{n+1} in two steps. First, evaluate hyperbolic parts (minimum variance term) using methods described in [19]. For the hyperbolic part in Equation 2.52 the Hamilton-Jacobi level

```
$i \leftarrow 1$
Initialize $\phi$ to a signed distance function.
while $|\phi^n - \phi^{n+1}| > \epsilon$ do
    Compute means $\mathbf{c_1}$ and $\mathbf{c_2}$ using Equations F.18c and F.18d
    if mod $(i, \theta) == 0$ then
        Find curvature $\kappa$ of $\phi$ and calculate $\kappa g$.
        Find normals $\mathbf{n}$ of $\phi$ and calculate $\langle \nabla g.\mathbf{n} \rangle$
    end if
    Calculate $\mathbf{H_1}$, $\mathbf{H_2}$ and $\mathbf{H_3}$ using Godunov Scheme
    Calculate $\Delta t$ using Equation 2.56
    $\phi \leftarrow \phi^{n+1}$ (Equation 2.57), $i \leftarrow i + 1$
end while
```

Figure 2.7: Forward Euler Time Level Set Algorithm

set methods are used. Alternatively, the equation could be simplified replacing $|\phi| = 1$ since ϕ is signed distance it is considered a good approximation and time step is predetermined by the user as a parameter. Then hyperbolic part reduces to:

$$\phi^{int} = \phi^k + \Delta k \beta \Big[(c_1 - c_2)(I - \frac{c_1 + c_2}{2}) \Big]. \tag{2.58}$$

where k is time, Δk is time step and ϕ^{int} is the intermediate result that will be used in next equation:

$$\phi^{k+1} = (I - \Delta k A_1)^{-1} (I - \Delta k A_2)^{-1} (I - \Delta k A_3)^{-1} (\phi^i nt). \tag{2.59}$$

Here a problem arises: If ϕ^{int} is calculated using Hamilton-Jacobi methods, the time step will be calculated using CFL restriction. But for second part time step Δk is predetermined by user. So the equation is not solved in same time step (unlike the Explicit solution described in first part of this section). These solutions are different steps and can not be considered as one level-set solution [34]. For the intermediate part if simplified version (Equation 2.58) is used now same time step is used. This may cause algorithm produces instable results if enough diffusion is not introduced in mean curvature step [34]. Despite these theoretical drawbacks practically this method is still useful and converges faster, since it allows larger time steps (Numerical solution is unconditionally stable according to [19]).

The segmentation procedure is similar to one given in [34] for implicit model:

The segmentation algorithm for implicit model is given in Figure 2.8. For more details about updating step see Appendix G.

```
$i \leftarrow 1$
Initialize $\phi$ to a signed distance function.
while $|\phi^k - \phi^{k+1}| > \epsilon$ do
    Compute means $\mathbf{c_1}$ and $\mathbf{c_2}$ using Equations F.18c and F.18d;
    $\phi \leftarrow \phi^{int}$ ,Equation 2.58
    if mod $(i, \theta) == 0$ then
        Re-initialize $\phi$ to signed distance function
        $\phi \leftarrow \phi^{k+1}$ ,Equation 2.59
    end if
    $i \leftarrow i + 1$
end while
```

Figure 2.8: Backward Euler Time Level Set Algorithm

θ is a positive scalar and a variable parameter, in every θ steps GAC model is applied otherwise only Chan-Vese model (only variance term) is used to update ϕ.

The main segmentation part of the Level Set model has three versions:

- Standard-p,
- Standard-a,
- Adaptive,

where first one is standard model with predefined means, second one is the standard model with automatically calculated class means and third one is thickness adaptive model with predefined class means. In *standard-p*, means of *Muscle* and *Fat* classes are predefined and assumed to be same everywhere through out the volume. These mean intensity values for MR data (which are in [0 255] interval) are listed as: Muscle: 59 and Fat: 148; for CT data Muscle: 40 and Fat:-106 in Hounsfield Units (HU) scale. However, in *standard-a*, means of these classes are calculated in every step as described in Figure 2.7 and Figure 2.8. *Adaptive* also uses predefined mean values and is the subject of the next section.

All methods for main part is run for three dimension and two dimensions. Three dimensional versions of these method are tagged with ‘3D’ and two dimensional ones are tagged as ‘2D’ in Chapter 4. In ‘2D’ methods, Level Set equation is solved for each slice of the volume using only intra-slice information.

2.3.2.1 Adaptive Level Set Segmentation Model

Because of the partial volume problem thin muscles in the image have mean intensity close to the that of fat class. Henceforth the algorithm decides them as *Fat* class. The solution proposed in this study is to detect thin structures in every step and treat them differently. The segmentation method is described in Figure 2.9.

In every step, (after k-means initialization), algorithm finds thin structures using morphological opening. The voxels vanished during morphological opening operations are labeled as ‘Thin’. Other voxels are labeled ‘Non-Thin’. ‘Non-Thin’ regions are expanded using dilation operation. These voxels also labeled as ‘Non-Thin’. ‘Thin’ labeled muscle and fat classes are classified again using simple thresholding. These thresholds for ‘Thin’ structures are manually selected values. For CT data voxels with intensity values greater than -57.5 is classified as Muscle. For MR data, voxels which have intensity values in between 60 and 110 are classified as Muscle. This new initial segmentation for ‘Thin’ labeled voxels is to improve segmentation performance.

Afterwards, algorithm calculates minimum variance terms for two labels (‘Thin’ and ‘Non-Thin’) separately. For thin regions algorithm uses a predefined mean intensity value (MR: Muscle: 95, Fat: 137 (in grayscale unit); CT, Muscle: 7 HU, Fat: -106 HU). This is similarly expected to increase the accuracy in thin regions. The results are provided in Results Chapter 4.

2.3.3 Postprocess

Postprocess step has two parts. The first one is an optional step. The partial volume voxels on the boundary of fat and bone could have close intensity values similar to the *Muscle* class. These voxels are found in one voxel thickness interface between fat and bone. This problem arises both in MR and CT images since in both case muscle intensity value is between fat and

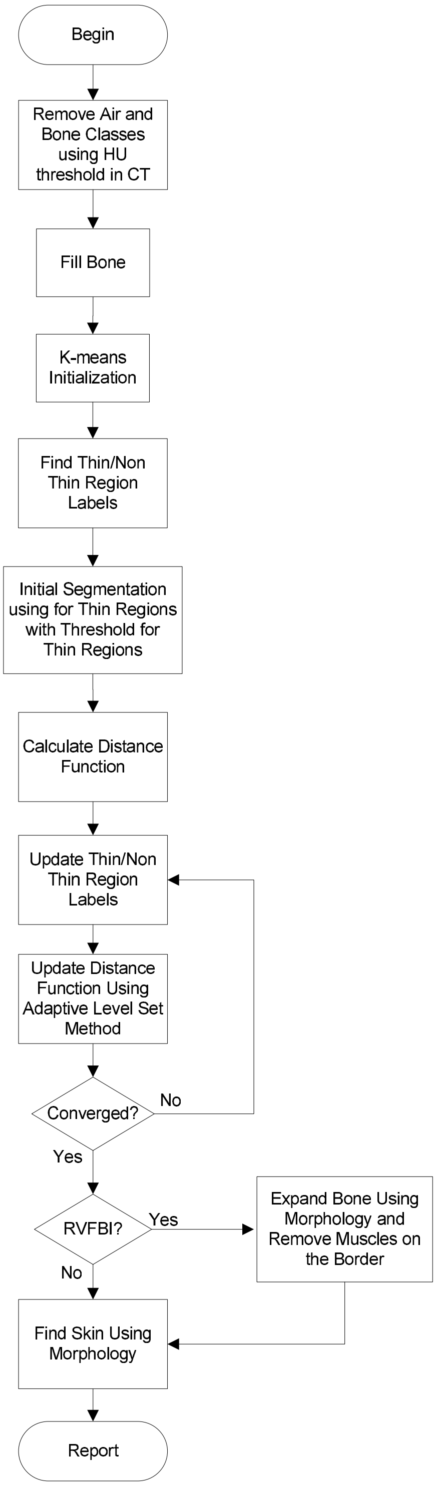

Figure 2.9: Thickness Adaptive Level Set (Forward Euler) Segmentation Method

bone. To alleviate this problem, smoothing (or diffusion) can be considered. This solution has a drawback: Thin muscle regions could also be vanished during smoothing . Since the position of these problematic voxels are well known on air-bone borders, expanding bone mask one voxel (using morphological dilate) is an alternate solution. This process will be called Removing Voxels on the Fat Bone Interface (RVFBI).

The second part of the Postprocess is to find Skin region. The skin is around 3-4 mms thickness for human which corresponds to approximately 4-5 voxels. Using this information, *Skin* is found using morphological operations. Erode function is a proper selection after image is binarized. Firstly, Air region is found using a proper threshold on CT image and then the remaining part is masked. However sinuses are filled with air and for that reason, if the image is eroded the structures that are not skin are also removed. To circumvent this problem, the mask is filled again using flood fill operation slice by slice manner and eroded to set the skin removed.

In this thesis, there are three types of main parts ('Standard-p', 'Standard-a' and 'Adaptive'). All these were solved in '3D' and '2D' and applied on three data cases (MR only, CT only and MR&CT unified), with RVFBI and without RVFBI options. In total there are 36 Level Set methods tested and compared on 16 ROI's.

2.4 A Bayesian Markov Random Field Segmentation Using a Partial Volume Model

Our Bayesian Markov Random Field (Bayesian MRF) segmentation model is an extension of the model described in [2]. They proposed a method for brain segmentation and we applied the method in [1] and [35] to segment non-brain parts of the head i.e. muscle, fat, bone tissues and air (both sinus and outside the head). The reason why we chose this method in [1][35] was that this method handles the partial volume classes. Partial Volume voxels are formed on the border of tissues during data acquisition and can be seen as a smooth transition in tissue neighborhoods in the MRI or CT data. Shattuck et. al.[2] classifies these partial volumes as different classes. Which gives a better classification performance. Below, the segmentation method of [2][1][35] is summarized and our extensions (adaptive segmentation) are explained.

Segmentation model is Maximum Aposteriori Probability (MAP) classifier based on Bayes Rule with Markov Random Field. The purpose is to find best label set Λ for the measurement set (image) X. MAP classifier is [2]:

$$p(\Lambda|X) = \frac{p(X|\Lambda)p(\Lambda)}{p(X)}. \tag{2.60}$$

The likelihood term ($p(X|\Lambda)$) is defined based on the assumption that voxels are independently distributed:

$$p(X|\Lambda) = \prod_{k\in\Omega} p(x_k|\lambda_k). \tag{2.61}$$

Where Ω is the voxel set, x_k is intensity values and λ_k is the label of each voxel. In [2] the likelihood term is defined for pure classes and partial volume classes. Pure classes are classes that contains only one class information. The pure classes in our Bayesian model are Bone, Muscle, Fat and Air. The partial volume classes (mixed classes) are the Fat-Muscle, Bone-Air, Fat-Bone, Muscle-Air, Muscle-Bone and Air-Bone. The likelihood term for pure class is:

$$p(x_k|\gamma) = \frac{1}{2\pi\sqrt{\sigma}} e^{-\frac{1}{2}\frac{(x-\mu)^2}{\sigma^2}} \tag{2.62}$$

Here, σ is standard deviation and μ is the mean of the gaussian distribution of the class which has the label γ. The likelihood for mixed classes is:

$$p(x_k|\gamma) = \frac{1}{2\pi\sqrt{\sigma_1}} \int_0^1 e^{-\frac{1}{2}\frac{(\alpha(x-\mu_1)-(1-\alpha)(x-\mu_2))^2}{\sigma_1{}^2}} d\alpha. \tag{2.63}$$

In Bayesian model, prior information is Gibbs prior (i.e. Markov Random Field - MRF) and calculated using potts model:

$$p(\Lambda) = \frac{1}{Z} exp\left[-\eta \sum_k \sum_{j\in N_k} \delta(\lambda_k, \lambda_j)\right]. \tag{2.64}$$

where δ is a simple comparison function, which is equal to -2 when labels λ_k and λ_j are equal, -1 when two labels have one common class and 1 otherwise, and η is an uniform, scalar weighting parameter. This prior probability is to hold connectivity in the segmented image.

The segmentation is obtained by finding the label set Λ maximizing MAP:

$$\Lambda^* = \arg\max(p(\Lambda|X)) \tag{2.65}$$

This problem is equal to:

$$\begin{aligned}\Lambda^* &= \arg\max(log(p(\Lambda|X))) \qquad (2.66)\\ &= \arg\max\left(log(p(X|\Lambda)) - \eta \sum_k \sum_{j\in N_k} \delta(\lambda_k, \lambda_j)\right)\end{aligned}$$

This optimization problem is difficult to solve with global optimization methods. Iterated Conditional Model (ICM) is a well known method for these kind of problems and was also used in [2][35][1]: In ICM the MAP probability of each voxel is calculated successively. The method usually converges in a few iterations.

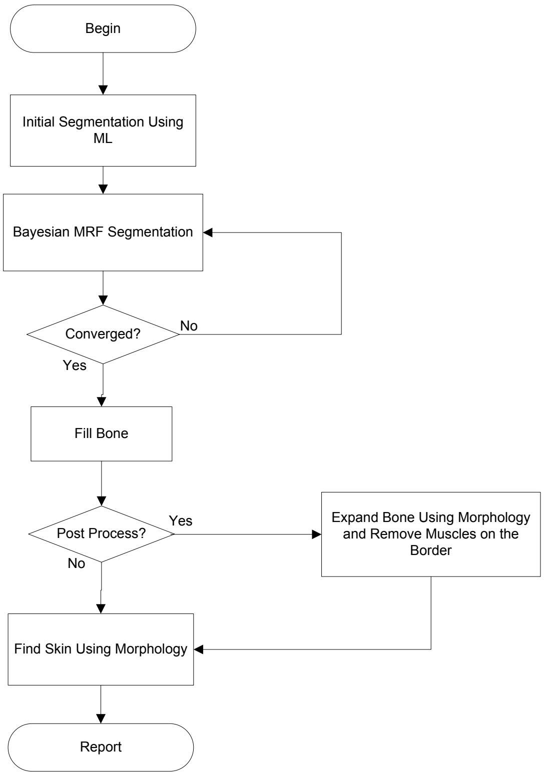

Figure 2.10: Standard Bayesian Segmentation Method

In the unified model case, vector valued data is defined. x_k is a two element vector such that $x_k = [x_{MR}, x_{CT}]^T$, where x_{MR} and x_{CT} are intensities of the k^{th} voxel. Then likelihood term is a multivariate Gaussian. For pure classes and mixed classes based on the fact that the covariance matrix of multivariate Gaussian is block diagonal (CT and MR are uncorrelated) they can be simplified as [2]:

$$p(x_k|\gamma) = \frac{1}{2\pi\sqrt{\sigma_{MR}\sigma_{CT}}} e^{-\frac{1}{2}\frac{(x_{MR}-\mu_{MR})^2}{\sigma_{MR}^2}} e^{-\frac{1}{2}\frac{(x_{CT}-\mu_{MR})^2}{\sigma_{CT}^2}} \qquad (2.67)$$

$$p(x_k|\gamma) = \frac{1}{2\pi\sqrt{\sigma_{MR}\sigma_{CT}}} \int_0^1 e^{-\frac{1}{2}\frac{(\alpha(x_{MR}-\mu_{MRA})+(1-\alpha)(x_{MR}-\mu_{MRB}))^2}{\sigma_{MR}{}^2}} e^{-\frac{1}{2}\frac{(\alpha(x_{CT}-\mu_{CTA})+(1-\alpha)(x_{CT}-\mu_{CTB}))^2}{\sigma_{CT}{}^2}} d\alpha. \tag{2.68}$$

Equation 2.68 is a mixture of Gaussian distributions of classes A and B. Subscripts in μ_{MRA}, μ_{MRB}, μ_{CTA} and μ_{CTB} denotes that mean value is the mean value of the subscripted class (A, B) in subscripted data (MR, CT). For example μ_{CTA} is the mean value of class A for CT data.

In this study, the Bayesian segmentation model classifies into four classes simultaneously. These classes are: **Fat**, **Air**, **Muscle**, **Bone**. *Bone* class includes marrow, skull and teeth and *Muscle* class contains blood vessels, glands and muscles. As in Level Set method, marrow tissue can easily be separated from the *Muscle* class by flood fill on the *Bone* as discussed above with one difference: This is done as a postprocess operation instead of preprocess because Bayesian method classifies also *Bone* class. The method uses its own *Bone* mask to find marrows.

The mean intensity values of four classes (which are in [0 255] interval) for MR data are: Air: 3, Bone: 18, Muscle: 59 and Fat: 148. For CT data Hounsield Unit (HU) scale is used. The HU values for four classes are given as: Air: -972, Bone: 1453, Muscle: 40 and Fat: -106.

An option to remove the partial volume voxels on the fat bone interface is also possible using Bayesian segmentation output of *Bone* labeled region.

2.4.1 Adaptive Bayesian Segmentation Model

The partial volume problem is again valid for the Bayesian model. A similar adaptive approach, as in adaptive Level Set Model Section 2.3.2.1 can be applied in here. In the Figure 2.11, proposed method is described. Different from the standard model described in the beginning of this section the voxels in the image are labeled as ‘Thin’ or ‘Non-Thin’ with the same technique described in Section 2.3.2.1. For these ‘Thin’ labeled regions, the method uses different mean intensity values (other than the values given above) for the muscle and fat classes. These values are Muscle: 95 and Fat: 137 for MR data and Muscle: 7 and Fat: -106 for CT data.

In Chapter 4 Standard Bayesian segmentation model will be called as, ‘Standard’ or ‘Bayesian

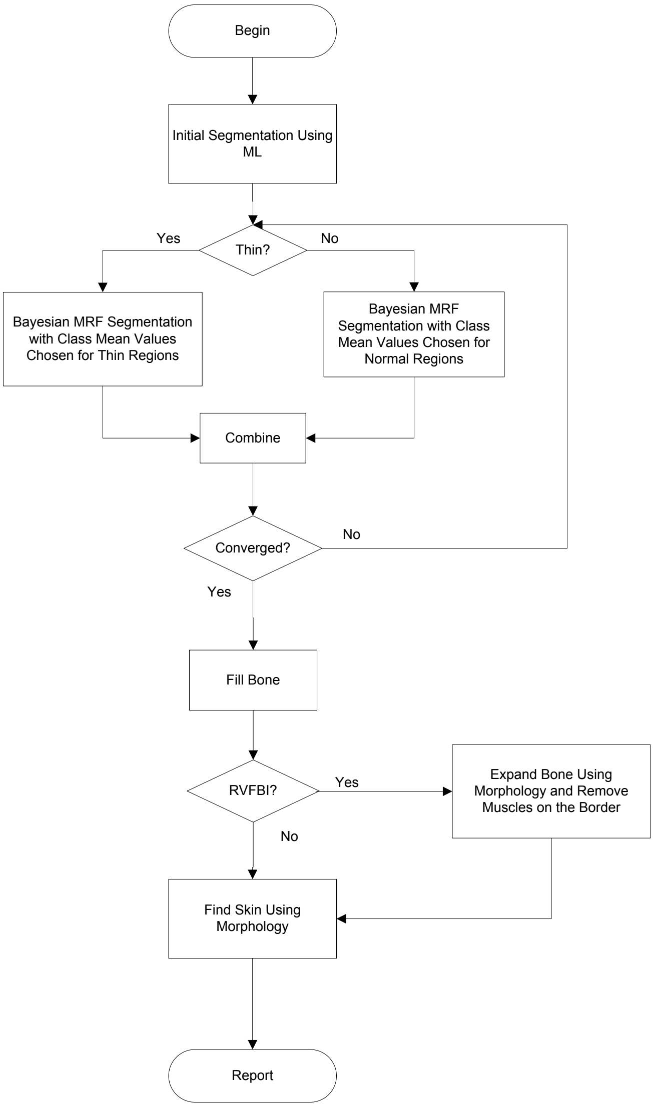

Figure 2.11: Adaptive Bayesian Segmentation Method

Standard' and adaptive Bayesian segmentation model will be called 'Adaptive' or 'Bayesian Adaptive'.

All Bayesian methods are run in three dimension and two dimensions. Three dimensional versions of these method are tagged with '3D' and two dimensional ones are tagged as '2D' in Results chapter (Chapter 4). In '2D' methods, Level Set equation is solved for each slice of the volume using only intra-slice information. Additionally RVFBI with and without options were tested separately.

All combinations give 24 Bayesian methods which were tested and compared on patient data.

CHAPTER 3

SIMULATION AND PATIENT DATA

3.1 Simulation

To optimize parameters (α, β γ and θ) for Level Set methods and (η) for Bayesian methods a realistic 3D synthetic data set is generated. The synthetic data is created such that it has thin muscle structures touching each other as in anatomy. The structures are defined as thin and long elliptical structures and created using an interface created in Matlab(R) environment. The bone, fat and air structures are spherical shapes centered on the lower right of the image with different radii (The image at the top in Figure 3.1). The muscle structures lay inside fat structure which is similar to the real anatomical structure of muscles.

The image noise is assumed to be normal distributed throughout the volume in MRI and CT. Homogeneous regions in real data were selected to identify mean and standard deviation values.

To simulate the PV affects three times upsampled volume of pure tissue classes are averaged. Finally, Gaussian noise is added using the standard deviation of the noise estimated. Since MR noise is uncorrelated for MR synthetic volume [2], randomly generated noise with zero mean is added. In CT volume, the noise is correlated [36]. This correlation is estimated and then randomly generated [37]. This process is illustrated in Figure 3.1. The images in the last row are synthetic images generated.

After creating the synthetic data, parameters of the models described in Chapter 2 were optimized using these synthetically created data. All parameter combinations cases were tested and best of the parameters were selected based on two metrics, discussed in the next section.

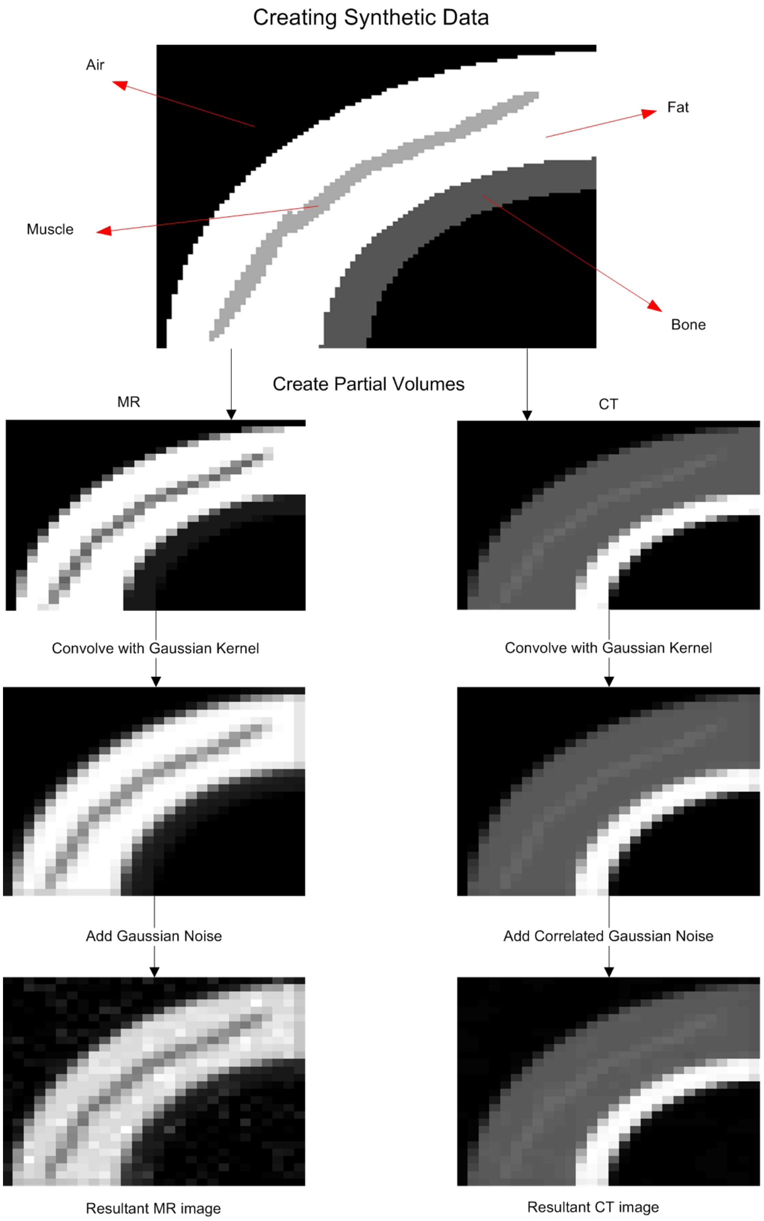

Figure 3.1: Steps of creating synthetic MR and CT images

3.1.1 Metrics

Two metrics are used while determining parameters. The first one is the Dice Coefficient (DC):

$$DC = \frac{2|S_1 \bigcap S_2|}{|S_1| + |S_2|}. \tag{3.1}$$

Where S_1 is the synthetic *Muscle* volume and S_2 is algorithmically segmented *Muscle* volume. If they are the same volume, the DC takes the value of 1. Otherwise, it takes a value between 0 and 1. The metric gives the ratio of overlapped volume to total volume of regions. However, this metric does not provide information about boundary accuracy of the segmentation.

The second metric used in this study compares boundaries of two label sets. It is called *Root Mean Squared Symmetric Surface Distance* (RMSSSD). It measures symmetric distance between two boundaries B_1 and B_2. The distance used in this study is Euclidian distance. The metric is calculated as follows: First, calculate $d_1 = dist(B_1, B_2)$ and $d_2 = dist(B_2, B_1)$ where d_1 and d_2 are squared symmetric distance arrays. $d_i(k)$ ($i = 1, 2$; $k \in N_i$ where N_i is the number of voxels on boundary B_i) is the minimum distance of the voxel k which belongs to set B_i to the boundary B_j ($j \neq i$). The d_1 and d_2 are combined to have d such that d is a vector. Finally, d is root mean squared which gives RMSSSD. This metric gives small values if two boundaries are close to each other. The metric is in Voxel units.

3.1.2 Parameter Optimization

The performance of each segmentation for a parameter set (α, β, γ and θ for Level Set methods and η for Bayesian methods) on the simulated images is ranked using both DC and RMSSSD metrics. It is a rating process:

1. Sort DC values in descending and RMSSSD values in ascending order.
2. Normalize all values such that:
    - Minimum DC value becomes zero and maximum DC value becomes N (number of parameter sets tested)
    - Minimum RMSSD value becomes N and maximum RMSSD value becomes zero.
3. Add these values to obtain ratings.
4. Choose parameter set with the highest rating.

All of the optimum sets are determined using this procedure and used in evaluations on patient data.

3.2 Ground Truth of Patient Data

Two data sets, each containing one CT and MRI volume, acquired from two patients were used in this study (Section 1.3, Appendix A). Sixteen ROI's (Region of Interest) which contain small muscle structures were selected to evaluate our methods. 11 ROI's were selected from the first data set. Remaining ROI's were selected from the other data set.

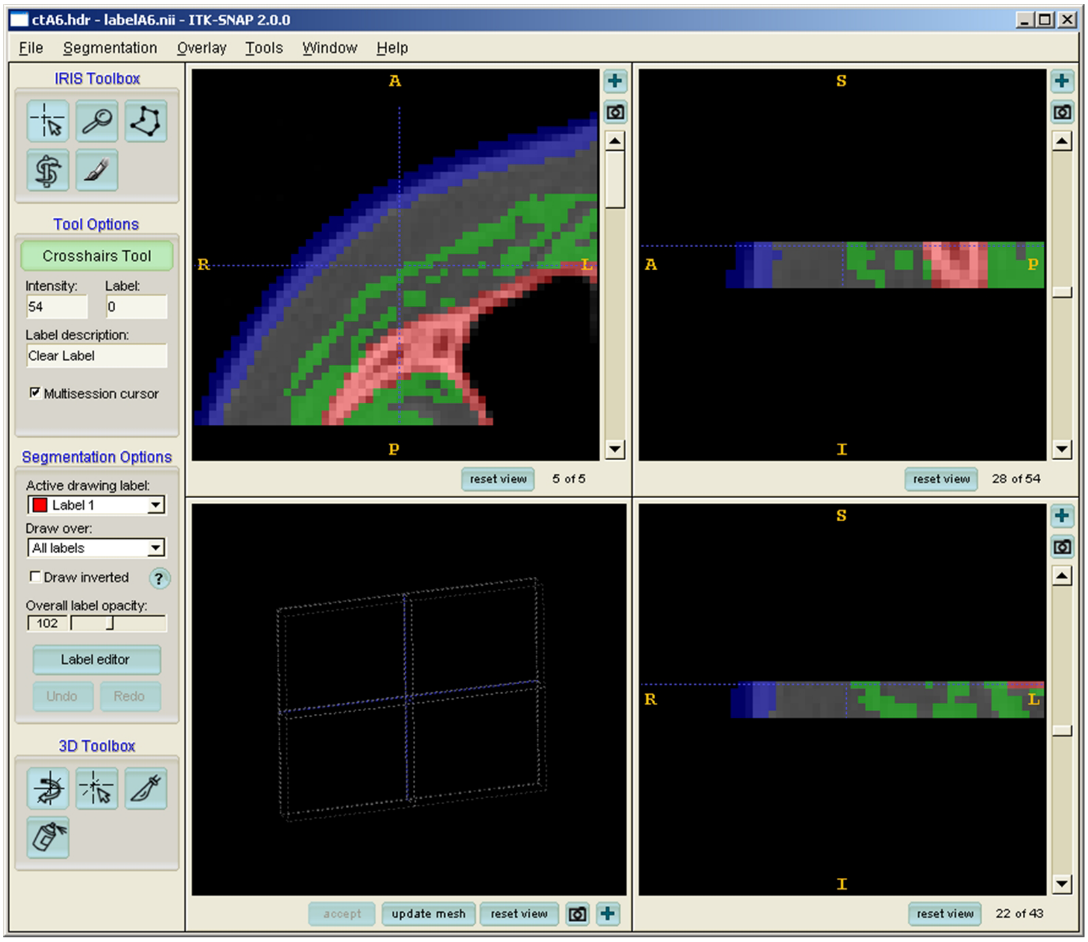

ctA6.hdr - labelA6.nii - ITK-SNAP 2.0.0

Intensity: 54
Label: 0
Label description: Clear Label
☑ Multisession cursor
Active drawing label: Label 1
Draw over: All labels
☐ Draw inverted
Overall label opacity: 102

Figure 3.2: Screen shot of the software program ITK Snap v 2.0. A CT volume is labeled. Red color is for *Bone*, Green is for *Muscle* and Blue is for *Skin*. Upper Left: axial view; upper right: sagittal view and lower right coronal view.

The ROI's were selected such that thin muscle structures exist. The ROI's were labeled by an expert viewing both modality, images side-by-side at the same time using a special software program (ITK Snap v 2.0 [24])is used. It is a software implemented using Insight Toolkit Library [23]. The software allows user to label the data with different colors. A screen shot of the software program is provided in Figure 3.2.

CHAPTER 4

RESULTS

4.1 Metrics and Statistical Analysis

The aim of this chapter is to quantitatively evaluate and compare the proposed methods by using the hand-segmented images as ground truth. Two metrics are used while evaluating methods as described in Section 3.1.1: The Dice Coefficient (DC) and Root Mean Squared Symmetric Surface Distance (RMSSSD).

Using these metrics, methods are evaluated and compared using paired t-test. Two tailed and one tailed paired t-tests are used. In two tailed test the null hypotheses H_0 is that means of two samples are equal. In one tailed test (depending on which tail is selected), the test is performed against the hypotheses: The mean of the one sample is greater/smaller than the other. The resulting statistics, p, is compared to the significance level (α). If p value is less than α, the null hypotheses is rejected. In one tailed test, this means that one sample has greater mean, and in two tailed test, it means that two samples have different means. $\alpha = 0.05$ is selected in this study.

While deciding whether a method is better than the other, two paired t-tests are used on DC and RMSSSD metric measurements. If the statistics of one of the metrics says two methods have unequal means in two-tailed tests then, of the two metric, the one which has smaller p value (one tailed test) is determined as a better result. The comparisons are made iteratively between each pair of methods to determine the best method. In the following section these statistical comparisons are given.

4.2 Comparison of Methods

While illustrating results two types of plot are used. The first one is mean ± standard deviation graph. In horizontal axis every element corresponds to a method and y axis is the metric value. The upper and lower limits are mean ± standard deviations and the dot in the middle represents means of the metric. The second one is the metrics versus ROI's. It shows what value metric takes in that ROI (horizontal axis of the plot).

The best result is found by following steps. First, for every segmentation family (Bayesian or Level Set), data groups (MR only, CT only and MR&CT cases) are evaluated within the group. Then these three methods (one from MR only case, one from CT only case and one from MR&CT unified case) are statistically compared and illustrated in figures. Finally, one from Level Set family and one from Bayesian family is determined as best and compared to each other.

There are 16 ROI's and 60 methods and 2 metrics, so when giving the results only some results, figures and images are provided. In illustrations, methods with abbreviation 'Y' (Yes) means RVFBI (Removing Voxels on the Fat Bone Interface) operation was applied. 'N' (No) means RVFBI (Removing Voxels on the Fat Bone Interface) operation was not applied. '3D' and '2D' indicates whether the method operated slice-by-slice manner or using volumetric information. In Level Set (LS) methods, abbreviation 'Standard-p' is used to name standard method using predefined class mean intensities and abbreviation 'Standard-a' is used for standard method using automatically (in every iterations) calculated class mean intensities and 'Adaptive' represents thickness adaptive Level Set model. Moreover, 'FE' stands for Forward Euler which represent forward euler time (explicit) solution of the Level Set equation. Similarly, for Bayesian methods, 'Standard' is used for standard Bayesian and 'Adaptive' is used for thickness adaptive model. See Section 2.3 and Section 2.4 for detailed explanation.

4.2.1 Bayesian with MRF Model Results

Figure 4.1 illustrates DC (Figure 4.1(a)) and RMSSSD (Figure 4.1(b))) metrics statistics (means ± standard deviation) applied to MR data. In Figure 4.1(a), it is observed the methods with RVFBI ('Y') have lower mean DC values than without RVFBI ('N') methods with no noticeable change for RMSSSD metric (Figure 4.1(b)). This is related with an anatomical fact: Muscles have facia tissue in and around. Bayesian method decides some voxels as bone in these regions since facia has intensity close to the bone intensity on MR. So if this bone region is expanded using morphology and the voxels around it is removed (RVFBI operation) many muscle voxels are lost which decreases the DC. Every ROI have this problem more or less. This is illustrated in Figure 4.2. In Figure 4.2(d) around the region inside the rectangle, the muscle is deleted because of the operation. While applying Bayesian model, in all ROI's method suffers from the same problem. This error does not exist in CT, because in CT modality facia has intensity much similar to that of muscle. In the unified scheme, Bayesian decision is in general correct.

For MR case, statistically, thickness adaptive model does not improve the performance. Standard models and adaptive models have equal means (DC, RMSSSD). Similarly '3D' and '2D' solutions of Bayesian methods have equal DC and RMSSSD means according to the t-test.

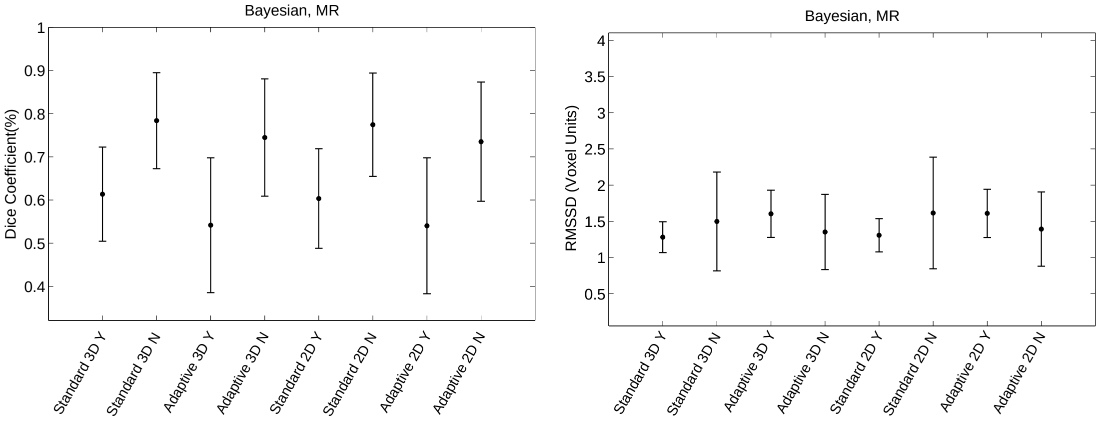

(a) (b)

Figure 4.1: Mean (Dice, RMSSSD) ± Standard deviation plot of metrics for 16 ROI's for 8 Bayesian methods applied to MR data (a) Dice Coefficients vs Methods. (b) RMSSSD vs Methods. 'Y': with RVFBI,'N': w/o RVFBI, Standard: Standard Bayesian with MRF, Adaptive: Thickness Adaptive Bayesian MRF, '3D': Three dimensions,'2D': Two dimensions.

Figure 4.3(a) is a graph to show Dice Coefficient metric statistics (mean ± Standard deviation) for 8 Bayesian methods applied to CT data. In Figure 4.3(b), RMSSSD statistics (mean± standard deviation) for 8 types of Bayesian method applied to CT data is illustrated. It is observed that methods with RVFBI give better results (higher mean DC and lower mean RMSSSD) and have smaller standard deviations in RMSSSD. Therefore it may be concluded

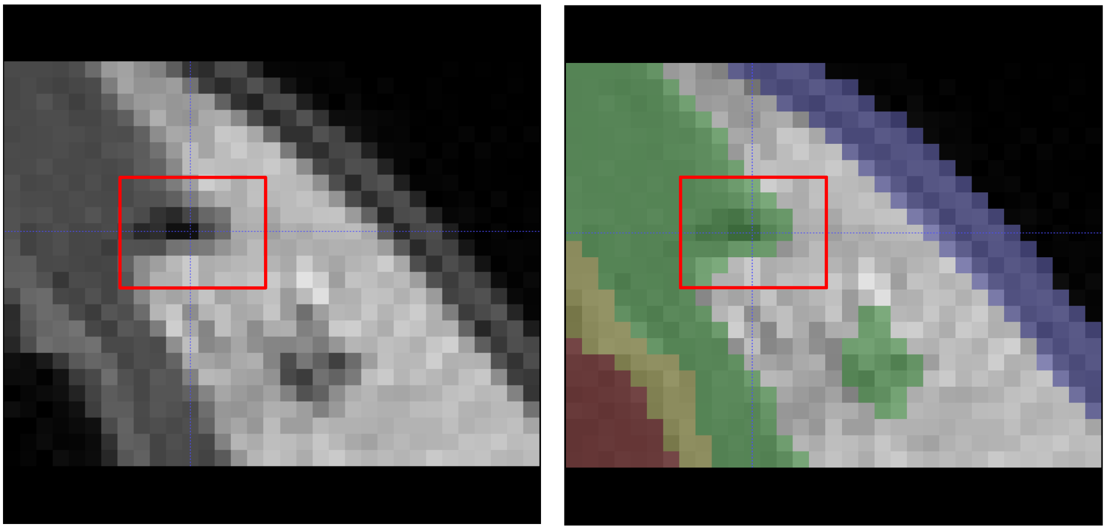

(a) Original MR

(b) Ground Truth

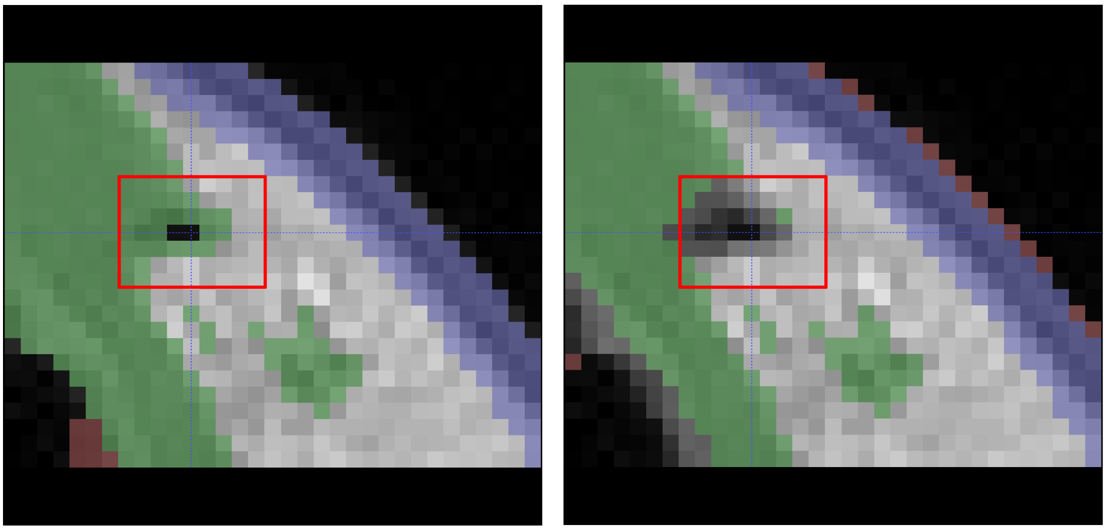

(c) 3D Bayesian Method Without RVFBI

(d) 3D Bayesian Method with RVFBI

Figure 4.2: (a) Original MRI Slice, (b) Its ground truth labels (c)3D Bayesian Method Without RVFBI, Note that the facia in the red rectangle is segmented as air. (d)3D Bayesian Method with RVFBI. The muscle voxels are removed because of RVFBI. Green is *Muscle*, Red is *Bone*, Blue is *Skin*, Black is *Air* and Non-labeled regions are *Fat* and Yellow designates soft tissue where intensity is close to *Muscle*

that results with RVFBI are better than results without RVFBI.

For the CT case, statistically, thickness adaptive model does not improve the performance. Standard models and adaptive models have equal means (DC, RMSSSD). Similarly ‘3D’ and ‘2D’ solutions of Bayesian methods have equal DC and RMSSSD means according to the t-test.

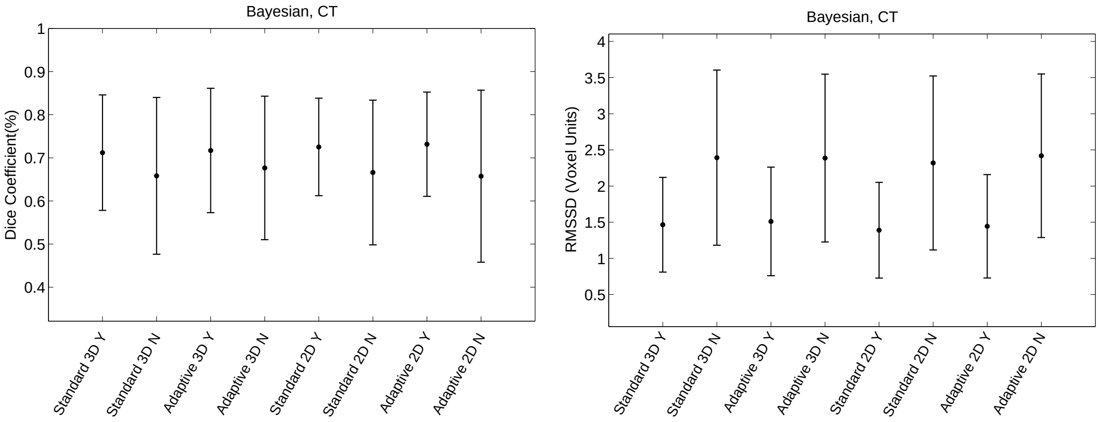

(a) (b)

Figure 4.3: Mean (Dice, RMSSSD) ± Standard deviation for 8 Bayesian methods applied to CT data (a) Dice Coefficients vs Methods. (b) RMSSSD vs Methods. Figure descriptions are same as Figure 4.1

Statistically best results for only MR (Figure 4.1) and only CT (Figure 4.3) case are as follows (also see Figure 4.5):

- For CT only:
    - Standard 3D Bayesian Method with RVFBI,
    - Adaptive 3D Bayesian Method with RVFBI,
    - Standard 2D Bayesian Method with RVFBI,
    - Adaptive 2D Bayesian Method with RVFBI,
- For MR only: Adaptive 3D Bayesian Model without RVFBI,
    - Standard 3D Bayesian Method without RVFBI,
    - Adaptive 3D Bayesian Method without RVFBI,
    - Standard 2D Bayesian Method without RVFBI,
    - Adaptive 2D Bayesian Method without RVFBI.

But none of the RMSSSD and DC metrics means of these two data cases are statistically different. In an example, paired t-test which compared Standard 3D Bayesian Method with RVFBI for CT case gave $p_{DC} = 0.1204 > 0.05$ and $p_{RMSSSD} = 0.8960 > 0.05$. This means that there is no difference in using MR or CT alone if one type of modality is available.

Figure 4.4(a) and Figure 4.4(b) depicts DC and RMSSSD metrics statistics for 8 Bayesian methods applied to MR&CT unified data. Results with RVFBI give better means and less variations.

For unified data case, statistically, thickness adaptive model does not improve the performance. Standard models and adaptive models have equal means (DC, RMSSSD). Similarly '3D' and '2D' solutions of Bayesian methods have equal DC and RMSSSD means according to the t-test.

Most successful methods are:

- Standard 3D Bayesian Model with RVFBI,
- Adaptive 3D Bayesian Model with RVFBI,
- Standard 2D Bayesian Model with RVFBI,
- Adaptive 2D Bayesian Model with RVFBI.

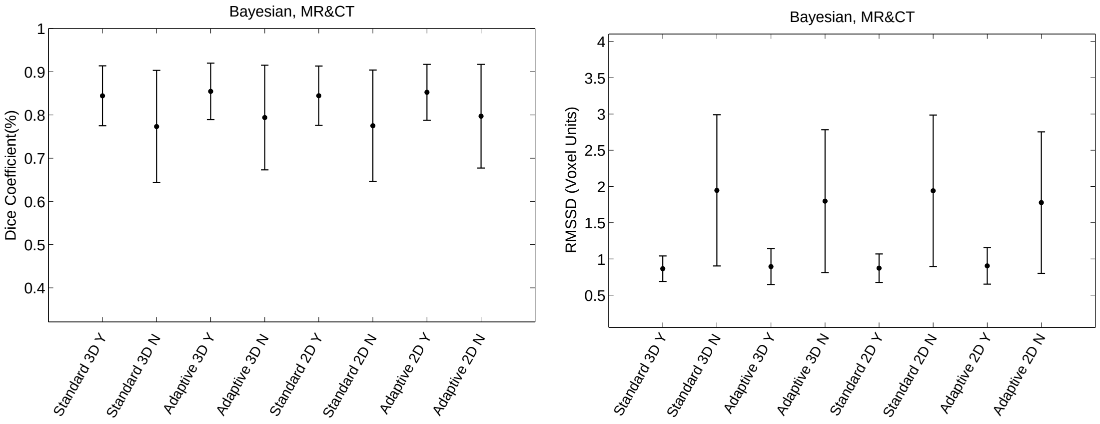

(a) (b)

Figure 4.4: Mean (Dice, RMSSSD) ± Standard deviation for 8 Bayesian methods applied to MR&CT data (a) Dice Coefficients vs Methods. (b) RMSSSD vs Methods. Figure descriptions are same as Figure 4.1

Two tailed t-tests shows that RMSSSD and DC means of these four methods are not statistically different (Table 4.1) but the 3D Adaptive case with RVFBI is chosen to be the best model with the comparison rule described in the beginning of this section. It can be concluded that methods with RVFBI is more accurate and precise than methods without RVFBI as observed in Figure 4.4.

Table 4.1: p values for paired t-tests for Bayesian methods with RVFBI applied to MR&CT unified data. Every p is greater than $\alpha = 0.05$, which means that are statistically not different from each other.

Bayesian with RVFBI	Std. 3D	Adap. 3D	Std. 2D	Adap. 2D
Std. 3D	-	0.68	0.99	0.75
Adap. 3D	0.68	-	0.69	0.93
Std. 2D	0.99	0.69	-	0.75
Adap. 2D	0.75	0.93	0.75	-

In Figure 4.5, metrics calculated from Bayesian methods of best methods of three groups (MR only (Figure 4.1), CT only (Figure 4.3) and MR&CT Figure 4.4 case) vs ROI's are plotted. Among all Bayesian methods, the best results are obtained by unified data case with 3D Adaptive with case with RVFBI (Figure 4.5). This result is expected because in this case more information is used to decide the voxel class (as mentioned earlier).

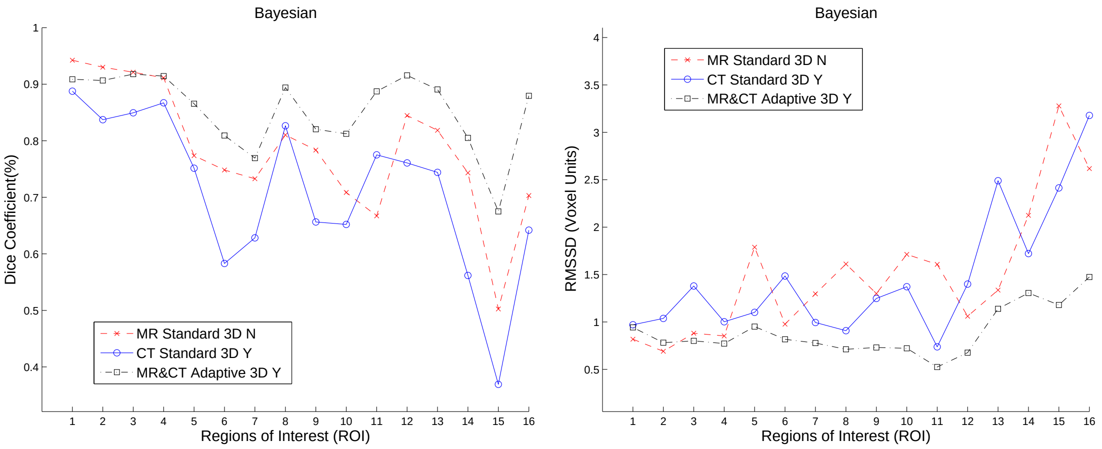

(a) (b)

Figure 4.5: Bayesian Metrics of best methods of three groups (MR only, CT only and MR&CT case) vs ROI's. (a) Dice Coefficients vs ROI's. (b) RMSSD graph vs ROI's.

Statistically, thickness adaptive model does not improve the performance. Standard models and adaptive models have equal means (DC, RMSSD). Similarly '3D' and '2D' solutions of Bayesian methods have equal DC and RMSSD means according to the t-test.

4.2.2 Level Set Model Results

Figure 4.6 and Figure 4.7 shows metric (DC and RMSSSD) statistics of 16 ROI's respectively, for 12 Level Set methods applied to MR only data and unified data cases. If *p* values are examined of these two cases (MR and MR&CT unified), it is observed that t-test fails to reject null hypotheses (methods' mean are same).

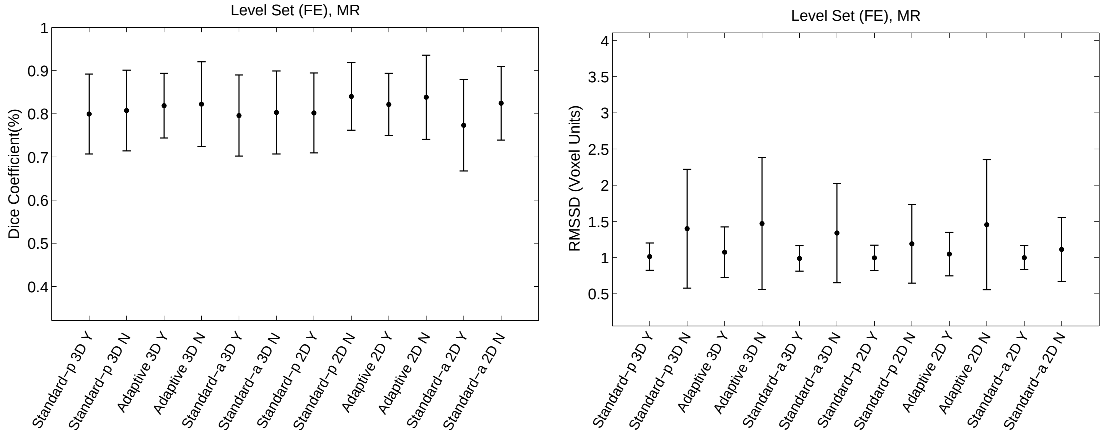

(a) (b)

Figure 4.6: Mean (Dice, RMSSSD) ± Standard deviation plot of metrics for 16 ROI's for 8 Bayesian methods applied to MR data (a) Dice Coefficients vs Methods. (b) RMSSSD vs Methods. 'Y': with RVFBI,'N': w/o RVFBI, Standard-p: Standard LS (FE) with predefined class means, Standard-a: Standard LS (FE) with automatic class means Adaptive: Thickness Adaptive LS FE,'3D': Three dimensions,'2D': Two dimensions.

Figure 4.8 shows means of both metrics of Level Set methods applied to CT only image is not as good as the other two cases. If these graphs are compared with the graphs illustrated in Figure 4.6 and Figure 4.7, it is observed that DC's are less than the other two groups and mean RMSSSD values are higher. In addition standard deviation is larger for CT only case. This poor performance with CT only data case can be as explained as follows: The edge information which is embedded in the process in the form of edge indicator function is not helping the level set function to be attracted by the edges of the image on a desired level. The smoothing effect (GAC model) on the model is more arbitrary and less edge dependent when compared with the case where MRI volume is involved. The CT data does not contribute to the segmentation, and hence MR only and MR&CT unified cases are not statistically different. This result can also be observed in Figure 4.9 which displays the calculated metrics of the best

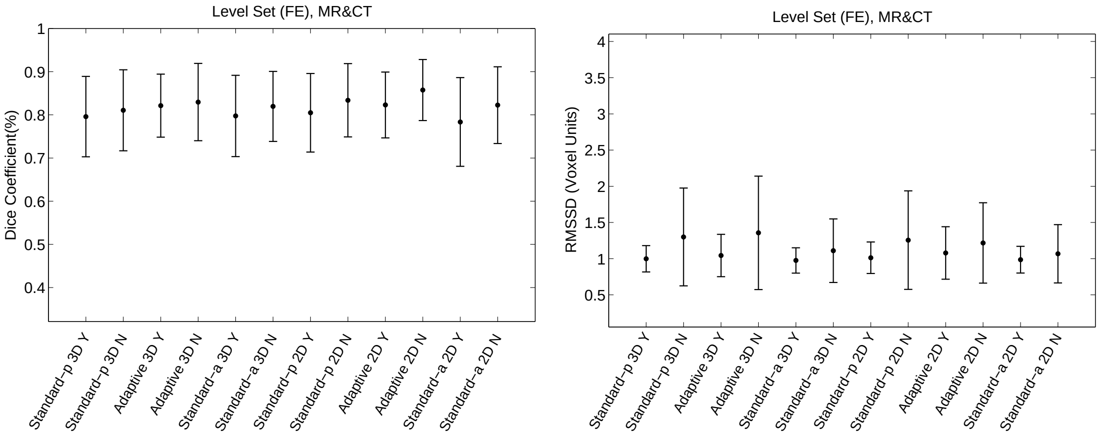

(a) (b)

Figure 4.7: Mean (Dice, RMSSSD) ± Standard deviation plot of metrics for 16 ROI's for 8 Bayesian methods applied to MR&CT data (a) Dice Coefficients vs Methods. (b) RMSSSD vs Methods. Figure descriptions are same as Figure 4.6.

methods vs ROI's of the three groups.

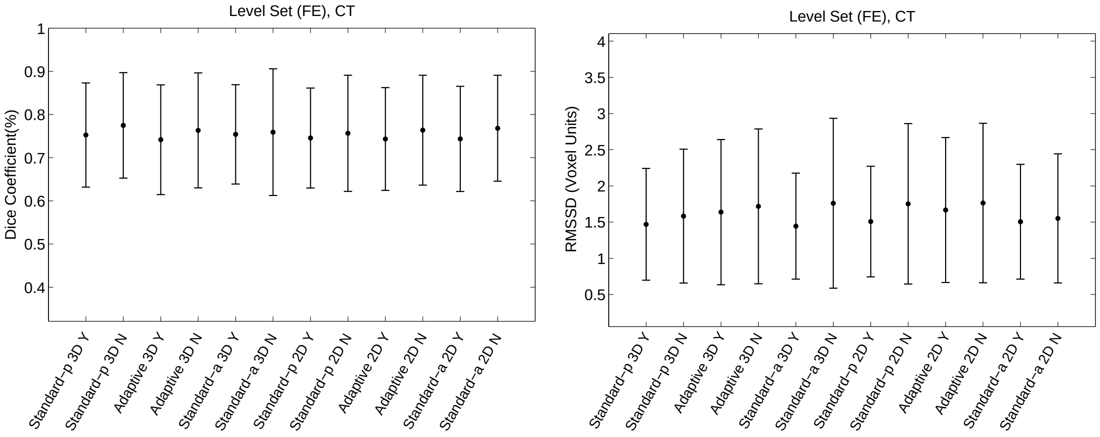

(a) (b)

Figure 4.8: Mean metrics (Dice, RMSSSD) ± Standard deviation plot of metrics for 16 ROI's for 12 Level Set methods applied to CT only data. (a) Dice Coefficients vs Methods. (b) RMSSSD vs Methods. Figure descriptions are same as Figure 4.6

The best method is found to be 3D Automatic method with RVFBI for Level Set, the results of this method have means equal to that of only MR case and MR&CT unified case except 3D Adaptive without RVFBI (the probability values ($p_{DC} = 0.48 > 0.05$ and $p_{RMSSSD} = 0.048 < 0.05$) shows that mean RMSSSD of 3D Automatic method with RVFBI is lower than mean RMSSSD value of 3D Adaptive without RVFBI). This concludes that Level Set model depends less on the chosen method. Choice of modality is more important and only RVFBI makes statistical difference (with RVFBI is better than without).

It is observed that ‘3D’ and ‘2D’ solutions of Level Set methods have no significant statistical difference. Similarly, Standard-a, Standard-m and Adaptive methods are in general have equal means for MR only and unified cases.

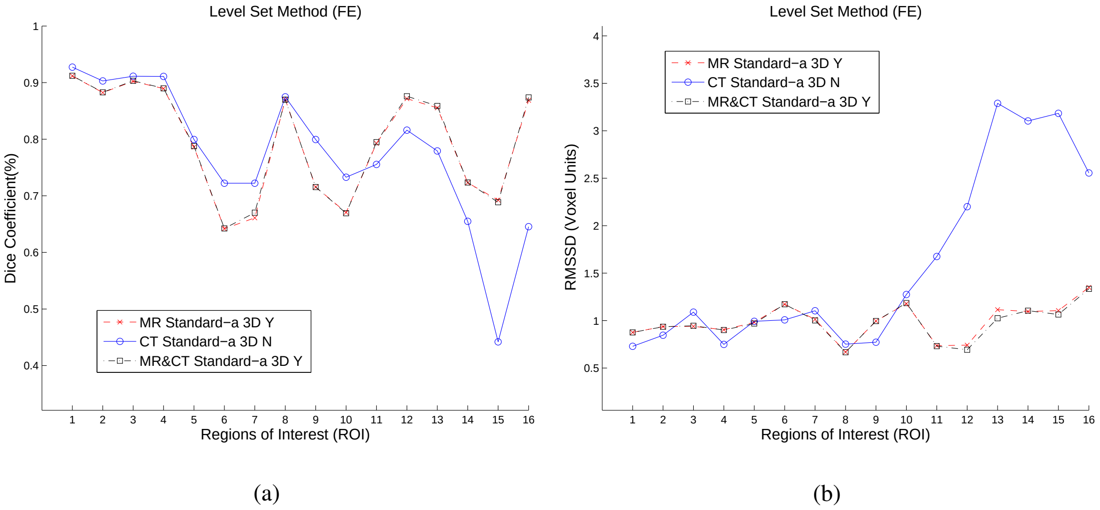

Figure 4.9: Level Set Metrics of best methods of three groups (MR only, CT only and MR&CT case) vs ROI’s. (a) Dice Coefficients vs ROI’s. (b) RMSSSD graph vs ROI’s.

The last comparison is between Bayesian and Level Set models (Figure). The best methods of two models are compared. They are Adaptive 3D Bayesian method with RVFBI applied to MR&CT data and Automatic 3D Level Set method with RVFBI applied to MRI&CT data. The null hypothesis is rejected i.e the mean Dice Coefficient of Bayesian group is greater than the Level Set group with $p_{DC} = 0.0086 < 0.05$. The mean RMSSSD values of two groups are statistically same. It is concluded that proposed Bayesian method is better than the proposed Level Set Method.

If only Dice Coefficient is considered than the best method is 2D Adaptive Level Set Method without RVFBI with a mean DC value of 0.86. If PV voxels on the fat bone borders are classified as *Muscle*, it increases RMSSSD. These misclassified PVs may not be important in the practical application because they are usually a few isolated voxels. Hence 2D Adaptive Level Set Method without RVFBI could be a matter of choice.

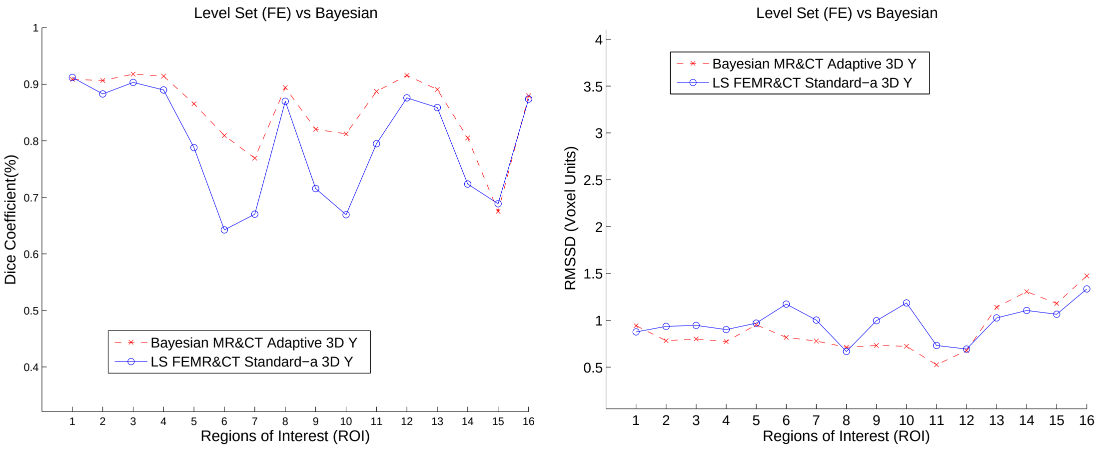

(a) (b)

Figure 4.10: The best of Level Set and Bayesian. (a) Dice Coefficients vs ROI's. (b) RMSSSD graph vs ROI's.

The tests are run in a computer with Intel(R) 2.53 GHz Cpu,and 2 Gbytes of RAM. All software is implemented and tested in Matlab 7.0.9.529, 2009b. The test results are given in Table 4.2 for a 43x35x35 voxel unit volume. In the table, elapsed time of 40 it (iterations) for Level Set methods and elapsed time for each iteration of Bayesian methods are given. Level sets converge at around 40 iterations and for Bayesian methods usually a few iterations (3-10) is enough. Note that Bayesian method segments into four classes while Level Set segments only muscle and fat classes. Hierarchial segmentation can be considered for segmenting into 4 classes [20]. These results show that Bayesian methods are advantageous in medical applications, in terms of both performance and computation speed.

Table 4.2: Run times (sec) for the methods. Measurements are for 40 iterations of Level Set method and for one iteration of Bayesian method. Single refers to CT or MR only data case and Unified refers to MR&CT case.

Method	Adaptive		Normal		Automatic	
	Single	Unified	Single	Unified	Single	Unified
3D Level Set time per 40 it.	6.43	6.44	7.3	7.5	6.3	6.3
2D Level Set time per 40 it.	4.5	4.8	4.9	5.1	4.37	4.3
3D Bayesian time per it.	0.15	0.19	0.37	0.41	-	-
2D Bayesian time per it.	0.15	0.19	0.37	0.41	-	-

Our observations on:

- 2D vs 3D method results: In general no statistical difference is found between these two type of approaches.

- Methods with vs without RVFBI: In general methods with RVFBI gives better results except for the Bayesian MR case (because of the facia tissue inside and around the muscles).

- Three data cases: Bayesian methods gives better results in unified case. Bests of MR only and CT only cases are statistically same. Level Set methods gives equal results for MR only and MR&CT unifed case. which are better than CT methods.

CHAPTER 5

CONCLUSIONS AND FUTURE WORK

5.1 Conclusion and Discussion

In this thesis the aim was to segment thin muscle structures using two types of segmentation models: Geodesic Active Contour Level Sets and Bayesian Markov Random Field with Partial Volume. These models have standard and thickness adaptive versions. They were applied for three data cases: MR only, CT only and MR&CT unified. Additionally, 3D and 2D versions of these methods were applied. In adaptive models, thickness of muscle structures were detected and class means were tuned for thin regions. These models included preprocess and postprocess steps (which contains simple image processing routines like morphological operations). Postprocess includes RVFBI (Removing Voxels on the Fat Bone Interface) which was considered an optional step, and skin removal.

For Level Set, Geodesic Active Contour model was used. It has a term minimizing integral of edge indicator function over the level set boundary, and it uses Chan-Vese model to find smooth regions. This model often stops in the local minima. In this study, a K-means initialization algorithm was used to prevent this, which provides a quicker convergence time.

Moreover, a simulation study was designed to optimize free parameters (α, β, γ and θ for Level Set and η for Bayesian) of methods in all combinations of 2D, 3D; with or without RVFBI; standard-a, standard-p, adaptive for Level Sets and standard, adaptive for Bayesian; CT only, MR only and unified (MR&CT) cases. To optimize these parameters, a synthetic data set (including an MR and CT volume) was created. Proposed methods were applied with different set of parameters to choose the best parameter set optimizing two metrics.

MR and CT data was hand-segmented by an expert radiologist to create ground truth. Proposed automatic segmentation method results were compared with ground truth data using Dice Coefficient (to measure volumetric segmentation accuracy) and Root Mean Squared Symmetric Surface Distance (to measure boundary segmentation accuracy). These metrics were compared statistically (using t-test) to determine the best method.

The 3D Adaptive Bayesian method with RVFBI applied on MR&CT unified case was observed to be the best method among Bayesian methods, however it is not statistically different from other Bayesian methods with RVFBI. Additionally, Bayesian MR&CT cases are better than individual image cases (MR only and CT only). It can be concluded that unifying data and RVFBI creates statistical difference for Bayesian segmentation model.

For the Level Set model, the best case is 3D Auto Level Set model with RVFBI using MR&CT unified case. Though, this model is found to be statistically no different from methods applied on MR case or unified data cases.

CT Level Set model resulted in the worst performance. We believe that the reason is that CT edge information does not contribute to the muscle segmentation model a lot. But in Level Set model CT is necessary in preprocessing operations to remove air and bone tissues (in CT images bone and air contrast is better than MR images).

Final comparison was made between the best Bayesian (3D adaptive with RVFBI applied on MR&CT) and the best Level Set (3D standard-a with RVFBI applied on MR&CT) methods. Bayesian method have higher Dice Coefficient mean than Level Set model (RMSSSD means of both groups are not different). Therefore we conclude that the Bayesian model is better than the Level Set in segmentation performance.

In addition, unified (MR&CT) data provides better segmentation accuracy as compared with single modality cases. However this depends on image registration accuracy. In fact, in our second data set, we observed some problems in CT-MR registration even with non-rigid techniques. This is why less number of ROI's were selected from second data set.

Moreover, our observations on 3D and 2D shows that these approaches are not statistically different. Similarly, adaptive methods are not better than standard methods, statistically.

Run times were also compared. The convergence time for the Level Set method was much higher than the Bayesian methods. Moreover, Bayesian model segments images into four classes, while Level Set model segments images into only two classes.

5.2 Future Work

Our measurements have shown that Bayesian methods converge faster than the Level Set methods. However Fast Marching algorithm [26] and GPU programming techniques can be used [38] to improve Level Set computation time.

To improve Level Set Segmentation performance, initialization independent methods which provides global minimization to the geodesic active contour model can be considered [39]. Improving edge information and modifying or changing the minimum variance term with a more efficient term [40] may also improve segmentation results. Hierarchical methods [20] can be used to segment all four classes which may improve the results. It is also possible to use air and bone segmentation results of Bayesian method to obtain a better air-bone mask.

To improve Bayesian segmentation performance prior models other than Gibb's prior can be explored.

Our methods (both Bayesian and Level Set) did not account for the differences in image resolution between MR and CT volumes. It is necessary to develop techniques to take into account resolution differences.

In addition, our tests were on two patient only. This is obviously not sufficient. Algorithm training on separate data set can be preferred.

Knowledge based supervised algorithms can also be considered for further improvements like [41]. However, human facial anatomy is very complex and there is wide variability along population which hinders generation of a statistical atlas.

Semi-automated methods are necessary to separate non-muscle tissue (glands and vessels) from the *muscle* class.

In this thesis, the effect of MR and CT artifacts due to implants and fillings was not investigated, and the subject of future studies.

REFERENCES

[1] Tübitak 1001, Proje No: 105E128, “Farklı görüntüleme tekniklerinin birleştirilmesi ile kişiye Özel sert ve yumuşak doku ile kişinin dış görünümünü İçeren 3b kafa modellenmesi ve bu modelin 3b görselleştirilmesi,” tech. rep., TUBITAK, 2008.

[2] D. W. Shattuck, S. R. Sandor-Leahy, K. A. Schaper, D. A. Rottenberg, and R. M. Leahy, “Magnetic resonance image tissue classification using a partial volume model,” *NeuroImage*, vol. 13, pp. 856–876, 2001.

[3] T. Tasdizen, D. Weinstein, and J. N. Lee, “Automatic tissue classification for the human head from multispectral MRI,” tech. rep., UCLA, 2004.

[4] “SCIRun: A scientific computing problem solving environment, scientific computing and imaging institute (SCI).”

[5] R. Olszewski, Y. Liu, T. Duprez, T. Xu, and H. Reychler, “Three-dimensional appearance of the lips muscles with three-dimensional isotropic MRI: in vivo study.,” *Int J Comput Assist Radiol Surg.*, vol. 4, pp. 349–52, 2009 Jun.

[6] E. Gladilin, S. Zachow, P. Deuflhard, and H. Hege, “Anatomy and physics-based facial animation for craniofacial surgery simulations,” *Medical & Biological Engineering & Computing*, vol. 42(2), pp. pp 167–170, 2004.

[7] Y. Kang, K. Engelke, and W. A. Kalender, “Interactive 3d editing tools for image segmentation,” *Medical Image Analysis*, vol. 8, no. 1, pp. 35 – 46, 2004.

[8] S. Beucher and C. D. M. Mathmatique, “The watershed transformation applied to image segmentation,” in *Scanning Microscopy International*, pp. 299–314, 1991.

[9] N. R. Pal and S. K. . Pal, “A review in image segmentation techniques,” *Pattern Recognition*, vol. 26, pp. 1277–1294, 1993.

[10] R. Adams and L. Bischof, “Seeded region growing,” *IEEE Trans. Pattern Anal. Mach. Intell.*, vol. 16, no. 6, pp. 641–647, 1994.

[11] N. Pal and S. Pal, “A review on image segmentation techniques,” *Pattern Recognition*, vol. 26, no. 9, pp. 1277–1294, 1993.

[12] E. C. Hildreth, “Theory of edge detection,” *Proceedings of the Royal Society of London. Series*, vol. 207, pp. 187–217, 1985.

[13] S. Osher and J. A. Sethian, “Fronts propagating with curvature dependent speed: Algorithms based on hamilton-jacobi formulations,” *Journal Of Computational Physics*, vol. 79, no. 1, pp. 12–49, 1988.

[14] D. Mumford and J. Shah, “Optimal approximations by piecewise smooth functions and variational problems,” *CPAM*, vol. XLII, no. 5, pp. 577–685, 1988.

[15] T. Chan and L. Vese, “Active contours without edges,” *Image Processing, IEEE Transactions on*, vol. 10, pp. 266 –277, feb 2001.

[16] V. Caselles, F. Catte, T. Coll, and F. Dibos, “A geometric model for active contours in image processing,” *NumMath*, vol. 66, pp. 1–31, 1993.

[17] R. Malladi, J. A. Sethian, and B. C. Vemuri, “Evolutionary fronts for topology-independent shape modeling and recovery,” in *ECCV ’94: Proceedings of the third European conference on Computer vision (vol. 1)*, (Secaucus, NJ, USA), pp. 3–13, Springer-Verlag New York, Inc., 1994.

[18] V. Caselles, R. Kimmel, and G. Sapiro, “Geodesic active contours,” *International Journal of Computer Vision*, vol. 22, pp. 61–79, 1995.

[19] R. Kimmel, “Fast edge integration,” 2003.

[20] M. Holtzman Gazit, R. Kimmel, N. Peled, and D. Goldsher, “Segmentation of thin structures in volumetric medical images,” *IP*, vol. 15, pp. 354–363, February 2006.

[21] J. B. G. Xiao, J. Noble, M. Burcher, and R.English, “Nonrigid registration of 3-d free-hand ultrasound images of the breast,” *IEEE Transactions on Medical Imaging*, vol. Volume 21, No. 4, pp. 405–412, 2002.

[22] N. Tustison, “N3 algorithm explanation:http://www.midasjournal.org/browse/publication/640.”

[23] L. Ibanez, W. Schroeder, L. Ng, and J. Cates, *The ITK Software Guide*. Kitware, Inc. ISBN 1-930934-10-6, http://www.itk.org/ItkSoftwareGuide.pdf, first ed., 2003.

[24] P. A. Yushkevich, J. Piven, H. Cody Hazlett, R. Gimpel Smith, S. Ho, J. C. Gee, and G. Gerig, "User-guided 3D active contour segmentation of anatomical structures: Significantly improved efficiency and reliability," *Neuroimage*, vol. 31, no. 3, pp. 1116–1128, 2006.

[25] M. Kass, A. Witkin, and D. Terzopoulos, "Snakes: Active contour models," *International Journal Of Computer Vision*, vol. 1, no. 4, pp. 321–331, 1988.

[26] J. A. Sethian, *Level Set Methods and Fast Marching Methods*. Cambridge University Press, 1999.

[27] S. Osher and R. Fedkiw, *Level Set Methods and Dynamic Implicit Surfaces*. Springer, 2002.

[28] X.-D. Liu, S. Osher, and T. Chan, "Weighted essentially non-oscillatory schemes," 1994.

[29] G.-S. Jiang, C.-W. Shu, and I. L, "Efficient implementation of weighted eno schemes," *J. Comput. Phys*, vol. 126, pp. 202–228, 1995.

[30] G.-S. Jiang and D. Peng, "Weighted eno schemes for hamilton–jacobi equations," *SIAM J. Sci. Comput.*, vol. 21, no. 6, pp. 2126–2143, 1999.

[31] R. P. Fedkiw, B. Merriman, and S. Osher, "Efficient characteristic projection in upwind difference schemes for hyperbolic systems (the complementary projection method," *J. Computational Physics*, vol. 141, pp. 22–36, 1998.

[32] C. P. Lee, *Robust Image Segmentation using Active Contours: Level Set Approaches*. PhD thesis, Department of Electrical and Computer Engineering North Carolina State University, 2005.

[33] E. Kreyszig, *Differential Geometry*. University of Toronto Press, 1959.

[34] F. E. Eric, F. Gibou, and R. Fedkiw, "A fast hybrid k-means level set algorithm for segmentation," tech. rep., 4th Annual Hawaii International Conference on Statistics and Mathematics, 2002.

[35] E. Şener, E. Mumcuoğlu, E. Kale, and V. Akgün, "BT ve MR görüntülerini 3 boyutta Çakıştırarak ve birlikte kullanarak, otomatik ve yarı-otomatik bölütleme yöntemleri geliştirilmesi ve bu yöntemlerin kafa modeli oluşturma ve yüz mimik kaslarının bölütlenmesine uygulanması," in *5. Ulusal Tıp Bilişimi Kongresi/Medical Informatics Turkey*, 2008.

[36] P. Razifar, M. Sandstrom, H. Schnieder, B. Langstrom, E. Maripuu, E. Bengtsson, and M. Bergstrom, "Noise correlation in PET, CT, SPECT and PET/CT data evaluated using autocorrelation function: a phantom study on data, reconstructed using FBP and OSEM," *BMC Medical Imaging*, vol. 5, no. 1, p. 5, 2005.

[37] E. Şener, *Automatic Bayesian Segmentation of Human Facial Tissue into Muscle/Fat/Bone/Air Classes using 3D MRI/CT Fusion By Incorporating Models of Measurement Degredation, Noise and Partial-Volume*. PhD thesis, Engineering Sciences Dept, METU, 2011 (Expected).

[38] A. Lefohn, J. E. Cates, and R. T. Whitaker, "Interactive, gpu-based level sets for 3d segmentation," in *In: Medical Image Computing and Computer Assisted Intervention (MICCAI*, pp. 564–572, 2003.

[39] X. Bresson, S. Esedoglu, P. Vandergheynst, J.-P. Thiran, and S. Osher, "Fast global minimization of the active contour/snake model," *Journal of Mathematical Imaging and Vision*, vol. 28, pp. 151–167, June 2007.

[40] A. Yezzi, Jr., A. Tsai, and A. Willsky, eds., *Medical Image Segmentation via Coupled Curve Evolution Equations with Global Constraints*, (Washington, DC, USA), IEEE Computer Society, 2000.

[41] O. Faugeras, R. Kikinis, and W. Wells, *Geometric Level Set Methods in Imaging, Vision, and Graphics*, ch. Knowledge-Based Segmentation of Medical Images, pp. 401 – 420. Springer-Verlag New York, Inc., 2003.

[42] H. W. Guggenheimer, *Differential Geometry*. McGraw-Hill (New York), 1963.

[43] S. Osher and N. Paragios, *Geometric Level Set Methods in Imaging,Vision,and Graphics*. Secaucus, NJ, USA: Springer-Verlag New York, Inc., 2003.

[44] J. P. Kaufhold, *Energy Formulations of Medical Image Segmentations*. PhD thesis, Boston University, 1995.

[45] J. Weickert, B. M. T. H. Romeny, and M. A. Viergever, "Efficient and reliable schemes for nonlinear diffusion filtering," *IEEE Transactions on Image Processing*, vol. 7, pp. 398–410, 1998.

APPENDIX A

PROPERTIES OF RADIOLOGICAL DATA AND ACQUISITION PARAMETERS

MR data is acquired by using Philips(R) Intera 1.5 Tesla (Philips Medical Systems, Best, Netherlands) device is used. The acquisition parameters are as follows:

- T1 3D FFE
- TR:25 ms
- TE:4.6 ms
- Slice Thickness:1 mm
- Slice Space:0.5 mm
- NSA:1
- FOV:230
- Matrix of:256 x 256
- Voxel Size :0.94 x 0.94 x 0.94 millimeters

These settings were recommended by MR scanner specialist.

Similarly, CT images are acquired by 16 channels multidetector computerized tomography device, Philips Mx8000 IDT (Philips Medical Systems, Best, Netherlands) is used for CT volume acquisition. Acquisition parameters for CT volume:

- 120 kiloVolt, 221 mAmper-secs.

- Rotation Time: 0.5 secs.
- Collimation: 16 x 0.75
- Slice Thickness: 1.5 mm
- Reconstruction Space: 0.75 mm
- Voxel matrix of: 25 x 25 cm and 512 x 512 voxels
- Reconstructed Voxel Size: 0.49 x 0.49 x 0.70 mms

After registration CT volume interpolated to the same voxel size as MR volume.

APPENDIX B

FORMAL DEFINITION OF LEVEL SET EQUATION

Suppose that $\Gamma(t = 0)$ is an $N - 1$ dimensional hyper-surface (curve in 2D and surface in 3D). And $\Gamma(t)$ is propagating with F along it's normal direction. In level set methodology this surface is considered to be the zero level set of an higher dimensional function ϕ Equation 2.1(a) and ϕ is defined,

$$\phi(x, t = 0) = \pm d \tag{B.1}$$

where x is a point in $\Re^N$(for example (x,y,z) in $\Re^3$) and d is the minimum Euclidian distance from x to $\Gamma(t = 0)$, and if x is negative inside Γ positive otherwise. Note that $d = 0$ on the hyper-surface. Then we have as given in [26],

$$\Gamma(t = 0) = [\{x|\phi(x, t = 0)\} = 0] \tag{B.2}$$

The aim is to write that equation for all t and find Γ as zero level set of the surface ϕ

$$\phi(x(t), t) = 0. \tag{B.3}$$

If this equation is differentiated with respect to t,

$$\phi_t + \nabla\phi \cdot x'(t) = 0 \tag{B.4}$$

where $x'(t)$ is defined as an external vector field. Equation B.4 is called ”convection equation” and it was examined in detail in Section 2.1.1. If we choose x as 2D vector we obtain,

$$\phi_t + \phi_x \cdot x_1'(t) + \phi_y \cdot y_1'(t) = 0 \tag{B.5}$$

If we replace x with a set of points which forms a curve in 2D and define the curve as,$C(t) = \langle x_1, x_2\rangle$ the level set Equation B.4 is rewritten for C,

$$\phi_t + \nabla\phi \cdot C_t(t) = 0. \tag{B.6}$$

Plugging $C_t = F \cdot n$ and $n = \frac{\nabla\phi}{|\nabla\phi|}$ in Equation B.4 leads to the equation,

$$\phi_t + F|\nabla\phi| = 0. \tag{B.7}$$

Although here C was chosen to be a curve in 2D, this equation is valid for arbitrarily chosen dimension. This is a general equation for N dimensions. It is possible to define vector x as an N dimensional vector and ϕ as $N + 1$ dimensional implicit function.

Alternatively if we define $\vec{V} = C_t(t)$ as an externally generated vector field and plug in to Equation B.6 we end up with,

$$\phi_t + \vec{V} \cdot \nabla\phi = 0, \tag{B.8}$$

which is the *convection* equation.

APPENDIX C

FIRST, SECOND AND THIRD ORDER HAMILTON-JACOBI NON OSCILLATORY NUMERICAL SCHEMES FOR SPATIAL DERIVATIVE

First, Second and Third order Hamilton-Jacobi Non Oscillatory Numerical Schemes (ENO1, ENO2 and ENO3) are numerical non oscillatory spatial approximations for Hamilton Jacobi equations like level set equation (2.1). They are derived from Newton divided differences. Except with a selective approach. The main idea is for second and order derivatives, to select the derivative side (right or left) which gives a smaller number i.e taking the information from the smooth side of the function. Lets start with Newton's divided difference scheme.

C.1 Interpolation Using Newton's Divided Difference Polynomial

In this method function is interpolated using a n^{th} order polynomial of the form:

$$f(x) = b_0 + b_1(x - x_0) + b_2(x - x_0)(x - x_1) + ... + b_n(x - x_0)(x - x_1)...(x - x_{n-1}) \tag{C.1}$$

where first three coefficient is given by:

$$b_0 = f(x_0) \tag{C.2}$$

$$b_1 = \frac{f(x_1) - f(x_0)}{x_1 - x_0} \tag{C.3}$$

$$b_2 = \frac{\frac{f(x_2)-f(x_1)}{x_2-x_1} - \frac{f(x_1)-f(x_0)}{x_1-x_0}}{x_2 - x_0} \tag{C.4}$$

These coefficients b_i are divided differences,

$$f[x_0] = f(x_0) \tag{C.5}$$

$$f[x_1, x_0] = \frac{f(x_1) - f(x_0)}{x_1 - x_0}. \tag{C.6}$$

Then the third divided difference is,

$$f[x_0, x_1, x_2] = \frac{f[x_2, x_1] - f[x_1, x_0]}{x_2 - x_0} \tag{C.7}$$

$$= \frac{\frac{f(x_1)-f(x_0)}{x_1-x_0} - \frac{f(x_2)-f(x_1)}{x_2-x_1}}{x_2 - x_0}. \tag{C.8}$$

Then if we sum up the results,

$$b_0 = f[x_0] \tag{C.9}$$

$$b_1 = f[x_1, x_0] \tag{C.10}$$

$$b_2 = f[x_2, x_1, x_0] \tag{C.11}$$

$$\vdots \tag{C.12}$$

$$b_n = f[x_n, ..., x_0], \tag{C.13}$$

where b_k is given,

$$b_k = \frac{f[x_k, ..., x_1] - f[x_{k-1}, ..., x_0]}{x_k - x_0}. \tag{C.14}$$

C.2 First, Second and Third order Essentially Non-Oscillator Schemes

Let's start zeroth divided difference

$$D_i^0\phi = \phi_i \tag{C.15}$$

which is the value of ϕ at the grid point x_i or at node i. First divided difference in the middle of the grid nodes is

$$D_{i+1/2}^1\phi = \frac{D_{i+1}^0\phi - D_i^0\phi}{\Delta x}. \tag{C.16}$$

Here $D_{i+1/2}^1\phi = D^+\phi_i$ and $D_{i-1/2}^1\phi = D^-\phi_i$. The second divided difference is defined as

$$D_i^2\phi = \frac{D_{i+1/2}^1\phi - D_{i-1/2}^1\phi}{2\Delta x}. \tag{C.17}$$

Finally the third divided difference,

$$D_{i+1/2}^3 = \frac{D_{i+1}^2\phi - D_i^2\phi}{3\Delta x} \tag{C.18}$$

is defined in the middle of the grid points. These divided differences are used to construct the polynomial

$$\phi(x) = Q_0(x) + Q_1(x) + Q_2(x) + Q_3(x) \tag{C.19}$$

where

$$Q_0(x) = \phi_i, \tag{C.20}$$

$$Q_1(x) = (D^1_{k+1/2}\phi)(x - x_i), \tag{C.21}$$

$$Q_2(x) = D^2_{k^*}\phi(x - x_k)(x - x_{k+1}), \tag{C.22}$$

$$Q_3(x) = D^3_{k^*}\phi(x - k^*)(x - x_{k^*+1})(x - x_{k^*+2}) \tag{C.23}$$

and subscripts k and m will be chosen according to ideas introduced in the beginning part of the section. To approximate ϕ_x the first derivative of the polynomial is calculated and evaluated at the grid point x_i.

$$Q_x(x_i) = Q'_1(x_i) + Q'_2(x) + Q'_3(x) \tag{C.24}$$

since $Q_0(x) = \phi_i$ and constant, it vanishes in the equation. If desired scheme is first order one should find Q'_1

$$\phi_(x) = (D^1_{k+1/2}\phi) \tag{C.25}$$

To obtain ϕ^+_x $k = i$, and to obtain ϕ^-_x $k = i - 1$ These are forward and backward schemes respectively that has been mentioned before. It is simply the upwinding scheme and named HJ ENO1, the one in the end denotes the order of the approximation. For a second order scheme Q'_2 should be considered. In the beginning of this section, it was mentioned that interpolation should be done in a smooth way and one of the operators (D^2_k) or (D^2_{k-1}) will be chosen. Smooth means less variation so, if $|D^2_k\phi| < |D^2_{k-1}\phi|$, $|D^2_k\phi|$ and $k = i$ is chosen or if $|D^2_k\phi| > |D^2_{k-1}\phi|$ $k = i - 1$ would be appropriate. Then $Q_2(x)$ is rewritten

$$Q_2(x) = c(x - x_k)(x - x_{k+1}) \tag{C.26}$$

with the introducing of variable c. c is either $D^2_k\phi$ or $D^2_{k-1}\phi$.

$$\begin{aligned} Q'_2(x_i) =& c((x_i - x_k) + (x_i - x_{k+1})) \\ Q'_2(x_i) =& c(i - k + i - k - 1)(\Delta x) \\ Q'_2(x_i) =& c(2(i - k) - 1)(\Delta x). \end{aligned} \tag{C.27}$$

If only Q'_1 and Q'_2 are used and Q'_3 is omitted we have second order scheme up to here and it is called HJ ENO2.

For third order approximation to calculate ϕ_x^+ and ϕ_x^- similarly $|D^3{}_k^* + 1/2|$ and $|D^3{}_k^* + 3/2|$ is compared and the smaller will be c^* in

$$Q_3(x) = c^*(x - x_k^*)(x - x_{k^*+1})(x - x_{k*+2}) \tag{C.28}$$

If we put Q'_1, Q'_2 and Q'_3 into the Equation C.24, third order HJ ENO approximation is obtained.

APPENDIX D

MEAN CURVATURE OF 3D AND 4D IMPLICIT FUNCTION

Curvature is a measure which gives how much the surface is bent at that point. For a point in the surface there are infinitely many tangent planes which includes different curvatures. The maximal and minimal of these curvatures are defined as principal curvatures and mean of these two curvatures κ_1 and κ_2 gives the mean curvature of a hypersurface at that point. For an implicit function ϕ, this value is related to the normal of the surface such as:

$$\kappa = \nabla \cdot \vec{N} \tag{D.1}$$

$$\kappa = \nabla \cdot \left(\frac{\phi(x)}{|\phi(x)|} \right) \tag{D.2}$$

For an 3D implicit function $\phi(x, y, z)$,

$$\kappa = \nabla \cdot \left(\frac{\phi(x, y, z)}{|\phi(x, y, x)|} \right) \tag{D.3}$$

$$= (\phi_x^2 \phi_{yy} - 2\phi_x \phi_y \phi_{xy} + \phi_y^2 \phi_{xx} + \phi_x^2 \phi_{zz} - 2\phi_x \phi_z \phi_{xz} + \tag{D.4}$$

$$\phi_z^2 \phi_{xx} + \phi_y^2 \phi_{zz} - 2\phi_y \phi_z \phi_{yz} + \phi_z^2 \phi_{yy}) / |\nabla \phi|^3 \tag{D.5}$$

And for 2D implicit function,

$$\kappa = \frac{\phi_x^2 \phi_{yy} - 2\phi_x \phi_y \phi_{xy} + \phi_y^2 \phi_{xx}}{|\nabla \phi|^3} \tag{D.6}$$

APPENDIX E

GEODESIC ACTIVE CONTOURS

$$E(C) = \oint_C g(C(s))\,ds \tag{E.1}$$

and since $ds = |C_p|dp$,

$$E(C) = \int_0^L g(C(s))\,ds = \int_0^1 g(C(p))|C_p|\,dp. \tag{E.2}$$

and $dp = \sqrt{x_p^2 + y_p^2}$ is substituted,

$$E(C) = \int_0^L g(C(s))\,ds = \int_0^1 g(C(p))|C_p|\,dp \tag{E.3}$$

If this integral is minimized w.r.t the evolving curve C, i.e. if the first variation of the integral is found:

$$\frac{\delta E}{\delta C} = \begin{pmatrix} \frac{\partial}{\partial x} - \frac{d}{dp}\frac{\partial}{\partial x} \\ \frac{\partial}{\partial y} - \frac{d}{dp}\frac{\partial}{\partial y} \end{pmatrix} (g(x(p), y(p))\sqrt{x_p^2 + y_p^2}). \tag{E.4}$$

For simplicity we solve the equation for only x component,

$$\frac{\delta E}{\delta x} = \frac{\partial}{\partial x} - \frac{d}{dp}\frac{\partial}{\partial y}(g(x(p), y(p))\sqrt{x_p^2 + y_p^2}) \tag{E.5}$$

$$= g_x|C_p| - \frac{d}{dp} g \frac{x_p}{\sqrt{x_p^2 + y_p^2}} \tag{E.6}$$

$$= g_x|C_p| - (g_x x_p + g_y y_p)\frac{x_p}{|C_p|} - g\frac{x_p|C_p| - x_p(x_p x_{pp} + y_p y_{pp})/|C_p|}{|C_p|^2} \tag{E.7}$$

and if we substitute $|C_p| = \sqrt{x_p^2 + y_p^2}$ and arrange the equation,

$$\frac{\delta E}{\delta x} = \frac{g_x x_p^2 + g_x y_p^2 - g_x x_p^2 - g_y y_p x_p}{|C_p|} - g\frac{x_{pp}x_p^2 + x_{pp}y_p^2 - x_p^2 x_{pp} - y_p x_p y_{pp}}{|C_p|^3}. \tag{E.8}$$

After canceling terms and taking into y_p parenthesis,

$$\frac{\delta E}{\delta x} = y_p(\frac{g_x y_p - g_y x_p}{|C_p|} - g\frac{x_{pp}y_p - x_p y_{pp}}{|C_p|^3}). \tag{E.9}$$

$\frac{g_x y_p - g_y x_p}{|C_p|} = -\langle \nabla g.n \rangle$

where $n = (-y_p, x_p)$ and curvature is defined as $\kappa = \frac{x_{pp}y_p - y_{pp}x_p}{C_p^3}$

then we end up with,

$$\frac{\delta E}{\delta x} = -y_p(\kappa g + \langle \nabla g.n \rangle) \tag{E.10}$$

for the variable y similarly one can derive $\frac{\delta E}{\delta y} = x_p((\kappa g - \langle \nabla g.n \rangle))$ then:

$$\frac{\delta E}{\delta C} = (\kappa g - \langle \nabla g \cdot \mathbf{n} \rangle)\mathbf{n} \tag{E.11}$$

And according to the steepest descent method $C_t = -\frac{\delta E}{\delta C}$ then:

$$C_t = -(\kappa g - \langle \nabla g.\mathbf{n} \rangle)\mathbf{n} \tag{E.12}$$

If in Equation E.12 we set $g(C(s)) = 1$ we come up with well known curvature flow:

$$\frac{\delta E}{\delta C} = -\kappa \mathbf{n} \tag{E.13}$$

The curve/surface moves in the gradient direction of the energy functional E (Steepest descent). By the time passes the Euclidian length of the curve is minimized in the fastest way by moving the curve by its own curvature. In other words boundary is being smoothed since large curvature means large speed and in the regions where there is high curvature shrinks faster than the other points. It is also called Euclidian Shortening Flow [42]. When $g = \frac{1}{1+|\nabla I(C(q))|}$ is used in E.12 curve/surface evolve in the direction of the gradient of energy function but now minimizing the edge indicator instead of the euclidian length. This curve evolution is called geodesic active contour/surface (GAC) . We can say curve evolves to maximize the gradient on it since minimizing $g(I)$ means maximizing the gradient from the integral. Then we have the following curve evolving equation:

$$C_t = (\kappa g - \langle \nabla g.\mathbf{n} \rangle)\mathbf{n} \tag{E.14}$$

and to write in level set form remember $\phi_t = -F|\nabla\phi|$ where $F = (\kappa g - \langle \nabla g.\mathbf{n} \rangle)$. and $\mathbf{n} = \frac{\nabla\phi}{|\nabla\phi|}$:

$$\phi_t = (\kappa g - \langle \nabla g.\frac{\nabla\phi}{|\nabla\phi|} \rangle)|\nabla\phi| \tag{E.15a}$$

$$\phi_t = \kappa g|\nabla\phi| - \langle \nabla g, \nabla\phi \rangle. \tag{E.15b}$$

APPENDIX F

MINIMUM VARIANCE TERM

$$E(C) = \int\int_{\Omega_C} f(x,y)dxdy \tag{F.1}$$

To find the first variation of this functional lets first examine the variation of an area integral.These kind region of functionals are given by:

$$E = \frac{1}{2}\int\int_{\Omega_C}(I - c_1)^2 dxdy + \int\int_{\Omega/\Omega_C}(I - c_2)^2 dxdy \tag{F.2}$$

The functions $P(x,y)$ and $Q(x,y)$ are defined as $P_y(x,y) = -\frac{1}{2}f(x,y)$ and $Q_x(x,y) = \frac{1}{2}f(x,y)$, then it is obvious that $f(x,y) = Q_x - P_y$. By using Green's theorem it can be rewritten as an contour integral:

$$E(C) = \int\int_{\Omega_C}(Q_x - P_y), dxdy = \oint_C (P, dx + Q, dy) \tag{F.3}$$

Change from x, y to arclength parametrization and writing in inner product form:

$$E(C) = \oint (Px_s + Qy_s), ds = \oint_C \langle\{-Q, P\}, \mathbf{n}\rangle, ds \tag{F.4}$$

The problem is changed into finding the first variation of the contour integral.

$$E(C) = \int_0^L \langle \mathbf{V}, \mathbf{n}\rangle ds = \int_0^L \langle\{u, v\}, \{-y_s, x_s\}\rangle ds \tag{F.5}$$

Now integration variable is changed to an arbitrary parametrization from arclength parametrization for generalization:

$$E(C) = \int_0^L \langle\{u, v\}, \{-y_s, x_s\}\rangle ds = \oint_0^1 \langle\{u, v\}, \frac{-y_p, x_p}{|C_p|}\rangle dp = \oint_0^1 (vx_p - uy_p)dp \tag{F.6}$$

And we can compute the first variation easily.

$$\frac{\delta E}{\delta C} = \begin{pmatrix} \frac{\partial}{\partial x} - \frac{d}{dp}\frac{\partial}{\partial x} \\ \frac{\partial}{\partial y} - \frac{d}{dp}\frac{\partial}{\partial y} \end{pmatrix} (vx_p - uy_p). \tag{F.7}$$

The first variation will be computed only for the variable x since, for the other variable the computation is very similar.

$$\frac{\delta E}{\delta x} = \frac{\partial}{\partial x} - \frac{d}{dp}\frac{\partial}{\partial y}(vx_p - uy_p) \tag{F.8}$$

$$= v_x x_p - u_x y_p - \frac{d}{dp}v \tag{F.9}$$

$$= v_x x_p - u_x y_p - v_x x_p - u_y y_p \tag{F.10}$$

$$= -y_p(u_x + v_y) = -y_p div((V)). \tag{F.11}$$

similarly,

$$\frac{\delta E}{\delta y} = x_p div((V))(n) \tag{F.12}$$

and finally the first variation of the contour integral is :

$$\frac{\delta E}{\delta C} = div((V))(n) \tag{F.13}$$

Then if $V = -Q, P$ defined, the variation of the region integral $E(C) = \int\int_{\Omega_C} f(x, y)dxdy$ becomes

$$\frac{\delta E(C)}{\delta C} = div(-Q, P)(n) = -(Q_x - P_y)(n) = -f(n). \tag{F.14}$$

For example if f is chosen to be constant, namely $f(x, y) = 1$ the curve will evolve according to the $C_t = \mathbf{n}$ in a constant speed in the normal direction, and will shrink like a balloon. It is so called balloon force, and indeed this evolution minimizes the area of the curve and the curve will shrink to the point and vanish.

Lets go back to the main equation the variance integration and arrange it:

$$E = \frac{1}{2}\int\int_{\Omega_C} (I - c_1)^2 dxdy - \frac{1}{2}\int\int_{\Omega/\Omega_C} (I - c_2)^2 dxdy + \frac{1}{2}\int\int_{\Omega} (I - c_2)^2 dxdy \tag{F.15a}$$

$$= \frac{1}{2}\int\int_{\Omega_C} (I - c_1)^2, dxdy - (I - c_2)^2 + \frac{1}{2}\int\int_{\Omega} (I - c_2)^2 dxsy \tag{F.15b}$$

With the first variation third term vanishes since it does not depend on C. The variation of the first term is obtained using the result from the variation of region integrals. If we replace $f(x, y)$ with $(I - c_1)^2 - (I - c_2)^2$ we end up with:

$$\frac{\delta E}{\delta C} = -(I - c_1)^2 - (I - c_2)^2 \tag{F.16}$$

or in a simple way by using the equality $(a - b)^2 - (c - d)^2 = (a + c - b - d)(a + d - b - c)$

$$\frac{\delta E}{\delta C} = (c_1 - c_1)\left(I - \frac{c_1 + c_2}{2}\right) \tag{F.17}$$

or in curve evolution formulation again the optimal c_1 and c_2 is obtained by taking the variations w.r.t c_1 and c_2 respectively.

$$\frac{\delta E}{\delta c_1} = \int\int_{\Omega} Idxdy - c_1 \int\int_{\Omega} dxdy = 0 \tag{F.18a}$$

$$\frac{\delta E}{\delta c_2} = \int\int_{\Omega_C} Idxdy - c_2 \int\int_{\Omega_C} dxdy = 0 \tag{F.18b}$$

$$c_1 = \frac{\int\int_{\Omega\setminus\Omega_C} Idxdy}{\int\int_{\Omega\setminus\Omega_C} dxdy} \tag{F.18c}$$

$$c_2 = \frac{\int\int_{\Omega_C} Idxdy}{\int\int_{\Omega_C} dxdy} \tag{F.18d}$$

Here, in equation (F.18c) the numerator value is the total intensity values of the image inside the boundary C, and denominator is the area (or volume for the 3D case) inside the boundary. Then the value c_1 is the average intensity value inside the boundary and similarly c_2 is the average intensity value of the image outside the boundary.

APPENDIX G

BACKWARD EULER TIME SOLUTION OF CURVATURE LIKE FORCES IN LEVEL SET EQUATIONS

For the implicit solution the Equation 2.52 has to be rearranged,

$$\phi_t \quad = \quad div\left(g(x,y,z)\frac{\nabla\phi}{|\nabla\phi|}\right) + \eta(\nabla\phi, I)|\nabla\phi| \tag{G.1}$$

$$\begin{aligned} \phi_t \quad = \quad & \frac{\partial}{\partial x}\left(g(x,y,z)\frac{\partial}{\partial x}\phi\right) + \frac{\partial}{\partial y}\left(g(x,y,z)\frac{\partial}{\partial y}\phi\right) \\ & + \frac{\partial}{\partial z}\left(g(x,y,z)\frac{\partial}{\partial z}\phi\right) + \eta(\nabla\phi, I) \end{aligned} \tag{G.2}$$

where,

$$\upsilon(\phi, \nabla I) = -\alpha I_{\xi\xi} - \beta g - \gamma\left((c_1 - c_2)(I - \frac{c_1 + c_2}{2})\right). \tag{G.3}$$

υ is combination of hyperbolic terms multiplied with $|\phi|$. In [43] $|\phi|$ was approximated $|\phi| = 1$ to make the calculations easier. Because in every iteration the implicit function is re initialized to signed distance and magnitude of gradient remains 1. So the term $|\nabla\phi|$ in Equation G.2 was dropped when writing Equation G.2. Let's define divergence operators,

$$A_1 = \frac{\partial}{\partial x}\left(g(x,y,z)\frac{\partial}{\partial x}\right) \tag{G.4}$$

$$A_2 = \frac{\partial}{\partial y}\left(g(x,y,z)\frac{\partial}{\partial y}\right) \tag{G.5}$$

and

$$A_3 = \frac{\partial}{\partial z}\left(g(x,y,z)\frac{\partial}{\partial z}\right). \tag{G.6}$$

To obtain implicit model, Equation G.2 is discretized in time using Forward Euler method,

$$\phi^{n+1} = \phi^n + \Delta t \sum_{l=1}^{3} A_l \phi^{n+1} + \Delta t \upsilon(\phi^n, I). \tag{G.7}$$

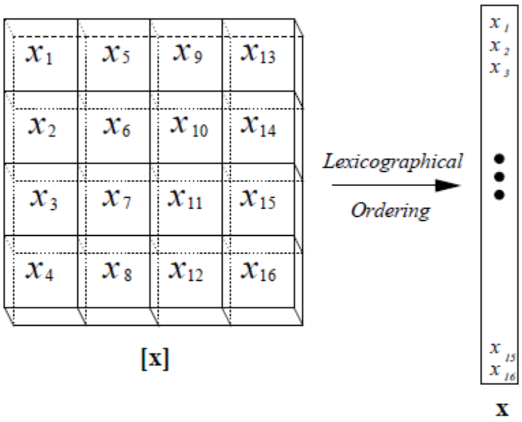

Figure G.1: Lexicographical ordering of an 2D matrix [44].

Here function ϕ is in vector form. And this vector is formed using lexicographical order as shown in Figure G for 2D image. The lexicographical order changes direction according to the operator acting. Discretization in one dimension (x) of divergence operator is [45], [19]

$$\frac{\partial}{\partial x}\left(g(x,y,z)\frac{\partial}{\partial x}\right) \approx \sum_{j\in N(i)} \frac{g_i + g_j}{h^2}(\phi_j - \phi_i). \tag{G.8}$$

N is 2 connected neighborhood of the current grid point i such as $N = i+1, i-1$. The divergence operators are tridiagonal matrices (see Appendix B) and the elements of are given:

$$a(i,j) = \left\{ \begin{array}{cc} \frac{g_i+g_j}{h^2} & j \in N(j) \\ \sum_{k\in N(k)} -\frac{g_i+g_k}{h^2} & j = i \\ 0 & \text{otherwise} \end{array} \right\} \tag{G.9}$$

To solve matrix this system, methods like Additive operator splitting (AOS) or Locally one-dimensional (LOD) schemes can be used. Here in this study, we followed [43] and used LOD. Then we have this resultant equation:

$$\phi^{n+1} = (I - \Delta t A_1)^{-1}(I - \Delta t A_2)^{-1}(I - \Delta t A_3)^{-1}(\phi^n + \eta(\nabla\phi^n, I)). \tag{G.10}$$

The entity $(I - \Delta t A_l)$ is tridiagonal and the solution of the system can be obtained using Thomas algorithm which makes calculations efficient.